The Astrophysical Journal, 777:34 (23pp), 2013 November 1 doi:10.1088/0004-637X/777/1/34
© 2013. The American Astronomical Society. All rights reserved. Printed in the U.S.A.

COMPOSITIONAL DIVERSITY IN THE ATMOSPHERES OF HOT NEPTUNES, WITH APPLICATION TO GJ 436b

J. I. Moses[1], M. R. Line[2], C. Visscher[3], M. R. Richardson[4], N. Nettelmann[5], J. J. Fortney[5],
T. S. Barman[6], K. B. Stevenson[7], and N. Madhusudhan[8]
[1] Space Science Institute, 4750 Walnut Street, Suite 205, Boulder, CO 80301, USA; jmoses@spacescience.org
[2] Division of Geological and Planetary Sciences, California Institute of Technology, Pasadena, CA 91125, USA
[3] Southwest Research Institute, Boulder, CO 80302, USA
[4] Rice University, Houston, TX 77005-1892, USA
[5] Department of Astronomy and Astrophysics, University of California, Santa Cruz, CA 95064, USA
[6] Lowell Observatory, Flagstaff, AZ 86001, USA
[7] Department of Astronomy and Astrophysics, University of Chicago, Chicago, IL 60637, USA
[8] Department of Physics and Department of Astronomy, Yale University, New Haven, CT 06520-8101, USA
Received 2013 June 21; accepted 2013 August 26; published 2013 October 11

ABSTRACT

Neptune-sized extrasolar planets that orbit relatively close to their host stars—often called "hot Neptunes"—are common within the known population of exoplanets and planetary candidates. Similar to our own Uranus and Neptune, inefficient accretion of nebular gas is expected produce hot Neptunes whose masses are dominated by elements heavier than hydrogen and helium. At high atmospheric metallicities of 10–10,000 times solar, hot Neptunes will exhibit an interesting continuum of atmospheric compositions, ranging from more Neptune-like, H_2-dominated atmospheres to more Venus-like, CO_2-dominated atmospheres. We explore the predicted equilibrium and disequilibrium chemistry of generic hot Neptunes and find that the atmospheric composition varies strongly as a function of temperature and bulk atmospheric properties such as metallicity and the C/O ratio. Relatively exotic H_2O, CO, CO_2, and even O_2-dominated atmospheres are possible for hot Neptunes. We apply our models to the case of GJ 436b, where we find that a CO-rich, CH_4-poor atmosphere can be a natural consequence of a very high atmospheric metallicity. From comparisons of our results with *Spitzer* eclipse data for GJ 436b, we conclude that although the spectral fit from the high-metallicity forward models is not quite as good as the best fit obtained from pure retrieval methods, the atmospheric composition predicted by these forward models is more physically and chemically plausible in terms of the relative abundance of major constituents. High-metallicity atmospheres (orders of magnitude in excess of solar) should therefore be considered as a possibility for GJ 436b and other hot Neptunes.

Key words: planetary systems – planets and satellites: atmospheres – planets and satellites: composition – planets and satellites: individual (GJ 436b) stars: individual (GJ 436b)

Online-only material: color figures

1. INTRODUCTION

Observations from the *Kepler* spacecraft reveal that planets with radii between that of the Earth and Neptune constitute a dominant fraction of the known transiting exoplanet population (Borucki et al. 2011; Howard et al. 2012; Batalha et al. 2013; Fressin et al. 2013). Most of these planets and planetary candidates orbit relatively close to their host stars and are therefore quite hot by solar system standards, with equilibrium temperatures $T_{\rm eq} \gtrsim 400$ K. These so-called hot Neptunes and hot Super Earths represent *terra incognita* for planetary researchers. The atmospheric compositions of these intriguing worlds could be widely diverse, ranging from the more familiar hydrogen-dominated ice-giant atmospheres, like our own Uranus and Neptune, to relatively hydrogen-poor CO_2-, H_2O-, or N_2-dominated atmospheres, or to even more exotic hot metallic, oxygen, and SiO-dominated atmospheres, depending on the planet's mass, effective temperature, formation history, atmospheric evolution, orbital parameters, and irradiation environment (Elkins-Tanton & Seager 2008; Schaefer & Fegley 2009; Kite et al. 2009; Rogers & Seager 2010b; Miller-Ricci & Fortney 2010; Rogers et al. 2011; Miguel et al. 2011; Miller-Ricci Kempton et al. 2012; Schaefer et al. 2012; Gaidos 2012; Hu et al. 2012).

We investigate the possible atmospheric diversity of hot Neptunes, i.e., close-in transiting exoplanets whose radii R_p are typically considered to fall in the $2\ R_\oplus < R_p < 6\ R_\oplus$ range (see Borucki et al. 2011; Howard et al. 2012), and whose atmospheres contain some H_2/He component. Our focus is on how atmospheric properties like temperature, metallicity, and bulk elemental ratios can affect the predicted equilibrium and disequilibrium composition of the atmospheres of generic hot-Neptune exoplanets, as well as specific hot Neptunes such as GJ 436b.

The discovery of GJ 436b by the radial-velocity technique (Butler et al. 2004; see also Maness et al. 2007), followed by its identification as a transiting planet (Gillon et al. 2007b), confirmed this intriguing object as the first Neptune-sized exoplanet ever detected. GJ 436b's mass of 1.4 $M_{\rm Nep}$ (0.078 $M_{\rm Jup}$, 25 $M_\oplus$), radius of 1.1 $R_{\rm Nep}$ (0.37 $R_{\rm Jup}$, 4.1 $R_\oplus$), and density of 1.2$\rho_{\rm Nep}$ (2.0 g cm^{-3}), according to von Braun et al. (2012), are all slightly larger than the corresponding values for Neptune. However, with an orbital semimajor axis of only 0.03 AU (Torres et al. 2008; Southworth 2010; von Braun et al. 2012), GJ 436b's dayside atmosphere maintains an effective temperature of ∼700–900 K (Deming et al. 2007; Demory et al. 2007; Stevenson et al. 2010; Madhusudhan & Seager 2011; Beaulieu et al. 2011; Knutson et al. 2011) as a result of the strong irradiation from its nearby M-dwarf host star, and thus the planet earns its "hot" designation. The planet's relatively large radius in relation to its mass suggests that GJ 436b, like Neptune, cannot be a purely rocky body or ocean world but must contain a non-negligible component of light gases like hydrogen and helium in an outer atmospheric envelope (e.g., Fortney et al. 2007; Deming et al. 2007; Gillon et al. 2007b; Adams et al. 2008; Baraffe et al. 2008; Figueira et al. 2009; Rogers & Seager 2010a; Nettelmann et al. 2010; Miller & Fortney 2011).

The spectral and photometric behavior of GJ 436b's atmosphere have been studied through secondary-eclipse observations in the 3.6–24 μm range (Deming et al. 2007; Demory et al. 2007; Stevenson et al. 2010; Beaulieu et al. 2011; Knutson et al. 2011) and through transit observations in the $\sim$0.5–8 μm range (Gillon et al. 2007a, 2007b; Deming et al. 2007; Alonso et al. 2008; Bean et al. 2008; Coughlin et al. 2008; Cáceres et al. 2009; Pont et al. 2009; Shporer et al. 2009; Ballard et al. 2010; Beaulieu et al. 2011; Gibson et al. 2011; Knutson et al. 2011; see also the recent *Hubble Space Telescope* (*HST*) Wide Field Camera 3 (WFC3) observations of H. A. Knutson et al. 2013, in preparation). Atmospheric models have been presented by Demory et al. (2007), Spiegel et al. (2010), Stevenson et al. (2010), Lewis et al. (2010), Madhusudhan & Seager (2011), Beaulieu et al. (2011), Shabram et al. (2011), Line et al. (2011), and Venot et al. (2013). The consensus from these models is that the large brightness temperatures derived from the *Spitzer* secondary-eclipse data are indicative of inefficient heat redistribution from the dayside to the nightside of the planet and that the atmospheric metallicity may be greater than solar.

More contentious are the compositional inferences from the transit and eclipse data for GJ 436b—the transit depths and their implications, in particular (cf. Pont et al. 2009; Beaulieu et al. 2011; Shabram et al. 2011; Gibson et al. 2011; Knutson et al. 2011). From analyses of transit spectra from *HST* NICMOS instrument in the 1.1–1.9 μm range, Pont et al. (2009) and Gibson et al. (2011) both conclude that the GJ 436b transit spectrum at these wavelengths is relatively flat, with no evidence for strong molecular absorption features (including those from water); however, the smaller-scale wavelength dependence of the transit depths are notably different in the two investigations. The recent *HST*/WFC3 observations of H. A. Knutson et al. (2013, in preparation) also confirm a relatively flat transmission spectrum in the 1.1–1.65 μm region. Analyses of transit photometric data from the *Spitzer* IRAC instrument at 3.6, 4.5, and 8 μm have led to the conflicting conclusions of a methane-rich atmosphere (Beaulieu et al. 2011) and methane-poor atmosphere (Knutson et al. 2011). As is discussed extensively in Knutson et al. (2011), the GJ 436b *Spitzer*/IRAC transit depths appear to vary with time, which despite the relatively old and apparently quiet nature of the host star, could be due to the occultation of star spots or other regions of non-uniform brightness on the star's surface as the planet transits across the disk. The eclipse data are less prone to such problems, although instrument systematics are still an issue, and stellar flares can complicate the data analyses (e.g., Stevenson et al. 2012). However, some disagreement still exists with respect to the inferred planetary flux at 3.6 and 4.5 μm and the associated error bars at these wavelengths in the eclipse data (cf. Stevenson et al. 2010, 2012; Beaulieu et al. 2011), although it is noteworthy that there is qualitative agreement in terms of the relative 3.6–4.5 μm flux ratio.

Resolving these discrepancies will be important (and/or obtaining new emission data for GJ 436b) because the *Spitzer* secondary-eclipse data at 3.6, 4.5, 5.8, 8.0, 16, and 24 μm suggest a very unexpected composition for GJ 436b's dayside atmosphere (Stevenson et al. 2010; Madhusudhan & Seager 2011). In particular, the very large flux in the 3.6 μm IRAC bandpass in combination with the negligible flux in the 4.5 μm bandpass suggest that CO and potentially CO_2 are much more abundant than CH_4 in the atmosphere of GJ 436b (Stevenson et al. 2010; Madhusudhan & Seager 2011; but see Beaulieu et al. 2011 for a contrary viewpoint), in contrast to theoretical equilibrium models (e.g., Lodders & Fegley 2002) that predict that CH_4 and H_2O will be the dominant carbon and oxygen constituents. If CH_4 were the dominant carbon-bearing species under GJ 436b photospheric conditions, then absorption in the 3.6 μm channel would be stronger than is observed, and the brightness temperature of the planet at those wavelengths would be much lower. Invoking a stratospheric temperature inversion in an attempt to explain the strong 3.6 μm emission does not improve the situation because the prominent ν_4 band of CH_4 would then produce a higher-than-observed flux at 8.0 μm (Stevenson et al. 2010; Madhusudhan & Seager 2011).

Through a systematic exploration of parameter space, Madhusudhan & Seager (2011) find that the best fit to all the *Spitzer* secondary-eclipse photometric data is obtained for atmospheres with very high CO mixing ratios, very low CH_4 mixing ratios, and moderately low H_2O mixing ratios, with no thermal inversion. Both Stevenson et al. (2010) and Madhusudhan & Seager (2011) suggest that non-equilibrium chemical processes could be responsible for this unexpected atmospheric composition, with photochemistry destroying the methane in favor of complex hydrocarbons and carbon monoxide, and transport-induced quenching in combination with a high-metallicity atmosphere allowing a large quenched CO abundance. However, Line et al. (2011) demonstrate that for assumed atmospheric metallicities up to 50 times solar, photochemistry does not effectively remove CH_4 from the GJ 436b's photosphere, and transport-induced quenching in combination with photochemistry cannot explain the large inferred CO/CH_4 ratio on GJ 436b. This result is confirmed by Venot et al. (2013). How then can the puzzling secondary-eclipse observations be explained?

We suggest that other bulk properties of the atmosphere, such as a very high metallicity or non-solar elemental compositions, could potentially resolve the current discrepancies between models and the secondary-eclipse observations of GJ 436b. As the atmospheric metallicity is increased in a planet with GJ 436b's effective temperature, the overall hydrogen mole fraction is decreased, and species like CO and CO_2 that do not contain hydrogen become progressively favored over hydrogen-containing species like H_2O and CH_4. Similarly, as the C/O ratio is decreased, CH_4 becomes progressively less important in relation to CO and CO_2 as a major carbon-bearing constituent (Madhusudhan 2012; Moses et al. 2013). We note that high-metallicity atmospheres are not unexpected for Neptune-mass planets (see Section 3.1 below). In fact, in our own solar system, Neptune's atmosphere is observed to have a C/H ratio of 40–120 times solar (Baines et al. 1995; Karkoschka & Tomasko 2011) and is estimated to have an O/H ratio greater than 400 times solar (Lodders & Fegley 1994; Luszcz-Cook & de Pater 2013).

We use both chemical-equilibrium models and thermochemical–photochemical kinetics and transport models (e.g., Moses et al. 2011, 2013; Visscher & Moses 2011) to investigate ways in which CO could be enriched at the expense of CH_4 in the atmosphere of GJ 436b. We also explore how bulk properties like atmospheric temperature, metallicity, and the

C/O ratio can affect the predicted composition of more generic hot Neptunes, leading to potentially widely diverse spectral properties for such planets.

2. THEORETICAL MODELS

2.1. Chemical Models

Two chemical models are used in this study. The first is a chemical-equilibrium model using the NASA CEA code of Gordon & McBride (1994), and the second is a one-dimensional (1D) thermochemical and photochemical kinetics and transport model based on the Caltech/JPL KINETICS code of Allen et al. (1981). The kinetics/transport model is described more fully in Moses et al. (2011), Visscher & Moses (2011), and Moses et al. (2013). For the equilibrium calculations, we consider ∼500 gas-phase species and condensates containing the elements H, He, C, N, O, Ne, Na, Mg, Al, Si, P, S, Cl, Ar, K, Ca, Ti, Cr, Mn, Fe, and Ni. For the kinetics/transport calculations, we solve the continuity equations for 92 atmospheric species via ∼1600 forward and reverse chemical-reaction pairs. Only species containing the elements H, He, C, N, and O are considered in the kinetics/transport model due to a lack of key rate-coefficient data for species containing the other elements. Note that the included elements are the dominant ones that will not be sequestered within condensates in the atmosphere of GJ 436b, and thus the GJ 436b results for the major gas-phase species are not expected to change significantly with the inclusion of additional elements.

The thermodynamic principle of microscopic reversibility, which is expected to be accurate even for complex multiple-potential-well chemical reactions (Miller et al. 2009), is assumed in the kinetics/transport model. Chemical equilibrium is achieved kinetically in the deepest, hottest regions of these models, but chemical reactions tend to be slower in the upper, cooler regions. When transport time scales drop below kinetic conversion time scales—at a pressure called the "quench pressure" or "quench level"—transport begins to dominate over chemical kinetics in controlling the species' vertical profiles (e.g., Prinn & Barshay 1977; Lewis & Fegley 1984; Fegley & Lodders 1994; Moses et al. 2010; Visscher & Moses 2011). When this situation occurs, the species can be "quenched" at mole fractions that remain constant with altitude above the quench level (and thus diverge from chemical-equilibrium predictions), as long as transport times scales remain shorter than chemical-kinetics time scales. Different assumptions about the rate coefficients for some key reactions can lead to differences in the predicted abundances of the quenched species (Visscher & Moses 2011; Venot et al. 2012); some of the current assumptions in published exoplanet models are reviewed by Moses (2013). The abundances of the carbon- and nitrogen-bearing species are particularly affected when kinetic interconversion between the dominant carbon constituents, CO and CH_4, and dominant nitrogen constituents, N_2 and NH_3, ceases to be effective.

Changes to the Moses et al. (2011) chemical mechanism, other than what is discussed in Moses et al. (2013), include the addition of O_3 and related reactions, which could potentially become important as the metallicity is increased. The rate coefficients and cross sections for these reactions are adopted from terrestrial atmospheric-chemistry compilations (e.g., Atkinson et al. 2004, 2006; Sander et al. 2011) and Venus photochemistry studies (e.g., Mills 1998). For the GJ 436b models discussed below, ozone does not build up to observable levels, and the added reactions do not measurably influence the observable species. Ions and ion chemistry are not included in the models, and our solutions at the highest altitudes in the model will be unrealistic due to our neglect of ion chemistry, high-temperature thermospheres, and possible hydrodynamic escape (e.g., García Muñoz 2007). The models contain 198 vertical levels separated uniformly in log pressure, with the hydrostatic equilibrium equation being used to solve for the background atmospheric parameters along the vertical grid. The chemical-equilibrium abundance profiles from the CEA code are adopted as initial conditions in the kinetics and transport models, with zero flux boundary conditions being assumed for all species at the top and bottom of the model. Our assumed solar composition is taken from the protosolar abundances listed in Table 10 of Lodders et al. (2009). Multiple Rayleigh scattering of incoming stellar radiation by gases is considered in the kinetics/transport models, but we assume that aerosols do not contribute to the atmospheric extinction.

We assume that vertical transport occurs through molecular and "eddy" diffusion, with the eddy diffusion coefficients K_{zz} being free parameters in the model. In the deep, convective portion of the atmosphere, free-convection and mixing-length theories (e.g., Stone 1976) predict relatively large eddy diffusion coefficients and short mixing time scales (e.g., $K_{zz} \approx 10^9$ cm^2 s^{-1} for the convective regions in GJ 436b), but K_{zz} values tend to be much smaller in the radiative regions in the upper troposphere and lower stratosphere. Higher up in the stratosphere, turbulence due to atmospheric tides and upward-propagating gravity waves (non-breaking as well as breaking waves) is expected to cause effective K_{zz} values to increase roughly with the inverse square root of atmospheric pressure (e.g., Lindzen 1981, and references therein)—a scaling that appears consistent with inferred vertical mixing in exoplanet general circulation models (GCMs; Parmentier et al. 2013; cf. also the K_{zz} profiles inferred from Showman et al. 2009, as shown in Moses et al. 2011). In our kinetics and transport models, the K_{zz} profile influences the quench behavior of molecules like CO, CH_4, and NH_3, and the observations themselves may ultimately provide the best means for defining both the K_{zz} values at the quench levels and the pressures at which those quench levels occur (e.g., Fegley & Lodders 1994; Bézard et al. 2002; Visscher et al. 2010b; Moses et al. 2010; Visscher & Moses 2011). However, the broadband photometric eclipse observations obtained to date for GJ 436b are not sufficient to constrain either the composition or thermal profile accurately enough to derive K_{zz} values in such a manner at this time. We therefore treat K_{zz} as a free parameter and will explicitly specify our assumptions for each model presented in Section 3.3.

2.2. Thermal Models

Both the chemistry and the predicted spectrum of our hot-Neptune exoplanets will depend strongly on the adopted thermal structure. We do not self-consistently calculate temperatures within the kinetics/transport models. For our generic hot Neptunes, we explore a wide range of temperature–pressure conditions. For GJ 436b, we consider a variety of theoretically derived thermal profiles, including the dayside-average profiles at conditions of secondary eclipse from the 1 times and 50 times solar-metallicity GCMs of Lewis et al. (2010), as shown in Figure 1. For higher-metallicity GJ 436b scenarios, we use the PHOENIX atmospheric model (Hauschildt et al. 1999; Allard et al. 2001) in the presence of an external radiation field, as described in Barman et al. (2001) and Barman et al. (2005), to compute 1D temperature–pressure profiles under the assump-

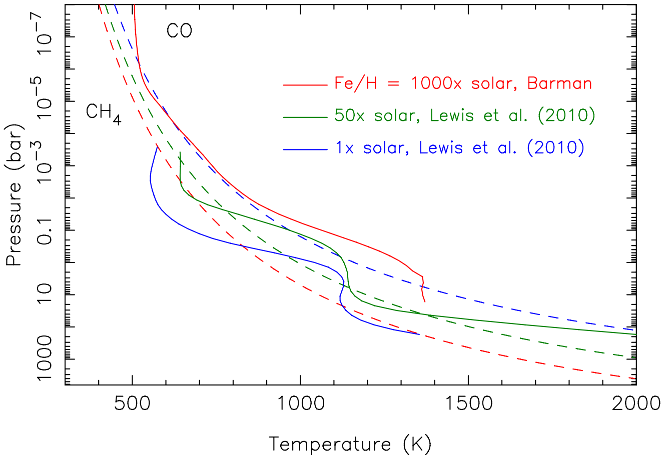

Figure 1. Theoretical thermal profiles (solid lines) for GJ 436b assuming various atmospheric metallicities. The profiles for 1 times solar metallicity (blue) and 50 times solar metallicity (green) are the atmospheric temperatures averaged over the dayside of GJ 436b at secondary-eclipse conditions from the GCMs of Lewis et al. (2010); the profile for 1000 times solar metallicity (red) is from a 1D, inefficient-heat-redistribution calculation based on Barman et al. (2005). The dashed lines represent the boundaries where CH_4 and CO have equal abundances in chemical equilibrium for the different metallicity models, with the color coding remaining the same as for the thermal profiles. Methane dominates to the lower left of these curves, and CO dominates to the upper right.

(A color version of this figure is available in the online journal.)

tion of inefficient day–night heat redistribution and efficient gravitational settling of condensates. The resulting profile for the case of 1000 times solar metallicity is shown in Figure 1. For all the non-solar-metallicity thermal models, solar ratios of elements other than hydrogen and helium are scaled by a constant factor. In certain instances, we also adopt thermal profiles from Madhusudhan & Seager (2011) that provide a good fit to the Stevenson et al. (2010) GJ 436b secondary-eclipse data, or we adopt profiles derived from new retrievals such as are described in Line et al. (2012, 2013; see also Section 3.2). We typically extend the thermal profiles upward in altitude nearly isothermally to a pressure of 10^{-11} bar, where all major UV absorbers are optically thin, and downward assuming an adiabat to a lower boundary that reaches at least 2400 K, to ensure that the N_2–NH_3 quench levels are contained within the models (i.e., to encompass the pressure at which kinetic interconversion between N_2 and NH_3 slows down enough to prevent equilibrium from being maintained, see Moses et al. 2010, 2011). The adopted thermal profiles will be clearly described when we discuss the different GJ 436b models.

Although the thermal profiles derived from the three-dimensional (3D) GCM and the 1D PHOENIX models have some notable differences for any given metallicity (not shown in Figure 1), both models predict a general upward vertical shift in the thermal profile as the metallicity is increased above solar. An increased metallicity results in increased mole fractions of opacity sources like water and other key molecular absorbers at lower pressures, which moves the optical-depth unity level (and "photosphere" in general) upward to higher altitudes. However, because the overall atmospheric number density decreases with increasing altitude, there is a limit to how high the photosphere can be shifted upward in altitude from this increased metallicity (see also Lewis et al. 2010; Miller-Ricci & Fortney 2010) because optical thickness cannot be approached at very high altitudes. As an example, the PHOENIX-based models show virtually no differences in the thermal profiles between 1000 times and 10,000 times solar metallicities. The chemical equilibrium CH_4-CO equal-abundance boundary also shifts downward in altitude with increasing metallicity (see Figure 1).

These two metallicity-dependent effects, first noted by Lodders & Fegley (2002) and discussed in relation to GJ 436b by Lewis et al. (2010), motivate our investigation and demonstrate why higher-metallicity models are more likely to explain the inferred large CO/CH_4 ratio needed to reproduce the secondary-eclipse data from GJ 436b (Stevenson et al. 2010; Madhusudhan & Seager 2011). For instance, Figure 1 illustrates that the thermal profile for the 1 times solar-metallicity model lies completely within the CH_4-dominated regime, so that no matter what the rate of vertical mixing or at what pressure the CO quenches, the carbon monoxide mole fraction will never exceed the CH_4 mole fraction for this solar-metallicity thermal profile. Because the dayside atmosphere is expected to be hotter than the terminators, the likelihood of having CO dominate at conditions relevant to the transit is even smaller if the atmosphere has a solar-like metallicity. In contrast, the thermal structure of the 1000 times solar model shown in Figure 1 lies completely within the CO-dominated regime, down to at least the 30 bar level. Since the CO–CH_4 quench point (i.e., where transport processes dominate over the chemical-kinetic interconversion of CO and CH_4) is likely to be within the ~0.1–30 bar region on GJ 436b (Moses et al. 2011; Visscher & Moses 2011; Line et al. 2011), the quenching will occur in the CO-dominated regime for the 1000 times solar-metallicity model, and carbon monoxide will dominate over methane.

In general, the hotter the photosphere of GJ 436b, the more abundant CO is likely to be. Aside from the effect of increased metallicities, hotter photospheres can result from the addition of tidal heating or a large residual internal heat source. GJ 436 is a relatively quiet star and slow rotator (Saffe et al. 2005; Demory et al. 2007; Jenkins et al. 2009; Sanz-Forcada et al. 2010; Knutson et al. 2010, 2011), suggesting that the system is relatively old (e.g., 6^{+4}_{-5} Gyr, according to Torres et al. 2008). For an older planet of GJ 436b's mass, the interior would be expected to have cooled significantly such that $T_{\rm int} \approx 60$ K for GJ 436b (comparable to that of Neptune with its $T_{\rm int} \approx 50$ K), defined in terms of an intrinsic internal heat flux of $\sigma T_{\rm int}^4$ (e.g., Fortney et al. 2007; Marley et al. 2007; Baraffe et al. 2008; Rogers & Seager 2010a). However, the orbit of GJ 436b has a significant eccentricity of 0.146 (von Braun et al. 2012), suggesting that the atmosphere is being tidally heated. Since orbital circulation times due to tidal dissipation are of order 30 Myr for GJ 436b (Deming et al. 2007), the eccentricity is likely being continually forced by one or more additional planets in the system (e.g., Deming et al. 2007; Demory et al. 2007; Stevenson et al. 2012). Depending on where the tidal energy is dissipated within the planet, the additional tidal heating could increase temperatures at the CO–CH_4 quench point, pushing the thermal profile into the CO stability field. Such a situation is shown in Figure 2 for a deep-seated intrinsic heat source on a 50 times solar-metallicity GJ 436b.

Note, however, that even the highest $T_{\rm int}$ profile shown in Figure 2 still resides close enough to the CO = CH_4 curve in the region from a few tens of bars to a few tenths of a bar that the quenched CH_4 abundance will be relatively large, even if CO dominates. For example, for the most favorable case of $T_{\rm int} =$ 300 K with vigorous mixing (e.g., $K_{zz} = 10^{11}$ cm^2 s^{-1}), which would result a quench point at relatively high temperatures and pressures, the quenched CH_4 mole fraction is 4×10^{-5}, which is a factor or 40 larger than the derived 1 ppm upper limit from *Spitzer* eclipse observations Madhusudhan & Seager (2011). A

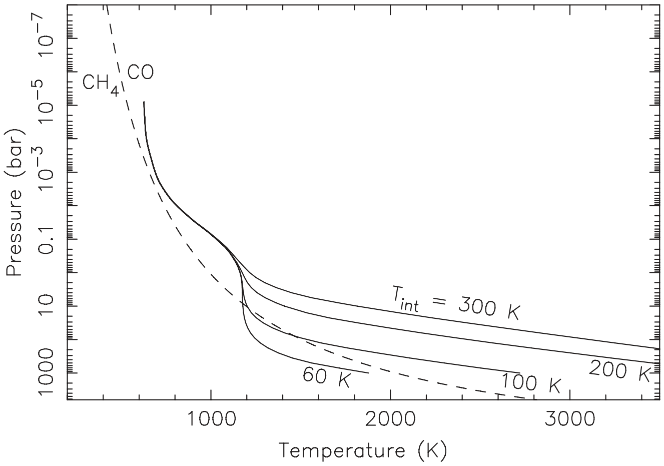

Figure 2. Theoretical thermal profiles for GJ 436b assuming different values for the intrinsic internal heat flux $F_{\rm int} = \sigma T_{\rm int}^4$, from 1D, 50 times solar-metallicity, inefficient heat redistribution calculations that are based on the models of Fortney et al. (2006, 2007).

higher metallicity *and* a large internal heat source would make higher CO/CH_4 ratios more likely.

2.3. Stellar Ultraviolet Flux

Another input to the kinetics/transport models is the ultraviolet flux from the host star, which has been classified in the literature as an early M dwarf of spectral type M2.5V to M3.5V (Kirkpatrick et al. 1991; Hawley et al. 1996; Maness et al. 2007; Jenkins et al. 2009). Figure 3 illustrates our adopted flux for GJ 436 (normalized to 1 AU), as derived from a compilation of various observational and theoretical sources. At wavelengths from 0 through the Lyman beta line at 1025.7 Å, we use the GJ 436 synthetic spectrum from the X-exoplanets archive at the Centro de Astrobiología (Sanz-Forcada et al. 2011), assuming the units in the downloadable file are photons $\rm cm^{-2}\ s^{-1}$ per wavelength bin, which then reproduces the correct integrated X-ray and EUV luminosity from Table 6 of Sanz-Forcada et al. (2011). At wavelengths between Lyman beta and the Lyman alpha line at 1215.7 Å, we use the solar spectrum of Woods & Rottman (2002) at solar-cycle minimum, scaled downward by a factor of 6.3 to transition smoothly to the longer-wavelength flux. For the Lyman alpha line itself, we use the reconstructed GJ 436 flux from Ehrenreich et al. (2011). For wavelengths between 1215.7 Å and 1800 Å, we use *International Ultraviolet Explorer* (*IUE*) data for GL 15B (a M3.5V star) from the MAST archive (http://archive.stsci.edu), and for wavelengths longer than 1800 Å, we use the spectrum of GL 15B from the Next Generation Spectral Library (Heap & Lindler 2010). For our dayside atmospheric models, we scale this normalized 1 AU spectrum to the 0.027 AU orbital distance relevant to the GJ 436b secondary eclipse. The key spectral region as far as the neutral atmospheric chemistry is concerned is the wavelength region from Lyman alpha out to ∼2400 Å. We use a fixed solar zenith angle $\theta = 48°$ to simulate the eclipse conditions in the calculations (see Moses et al. 2011). A directly measured ultraviolet spectrum for GJ 436 has recently been made available by France et al. (2013), and we emphasize that such studies are of great utility to theoretical photochemical models for exoplanets.

2.4. Spectral Models

To calculate the emergent planetary spectrum for GJ 436b from the assumed thermal structure and derived abundance profiles from the chemical models, we use a plane-parallel radiative-transfer code as described in Line et al. (2013). Opacity from H_2, He, H_2O, CO, CO_2, CH_4, and NH_3 is included in the modeling, although NH_3 itself is not included in the retrievals. The source line parameters are described in Line et al. (2013). Collision-induced absorption from H_2–H_2 and H_2–He is included in the models, but collision-induced absorption from other relevant collisional pairs such as H_2–CO, CO–CO, H_2O–CO is not. As atmospheric metallicity is increased, molecules like CO_2, CO, and H_2O increase in importance relative to H_2, and a future study of the full spectral effects of the changes in collision-induced absorption and overall continuum as the composition shifts would be interesting. Local thermodynamic equilibrium is assumed throughout, and scattering is ignored. In a manner similar to Sharp & Burrows (2007), absorption cross sections are precomputed using a line-by-line code at high spectral resolution and tabulated on a grid with 1 $\rm cm^{-1}$ wavenumber resolution and 20 evenly spaced temperature points between 500–3000 K and log(pressure) points between 50–10^{-6} bar (see http://www.atm.ox.ac.uk/RFM/). The cross sections from this pre-tabulated grid can then be interpolated for the pressure–temperature-abundance conditions relevant to the model atmosphere, which has 90 grid layers equally spaced between 50–10^{-6} bar. As is typical, we plot the model emission spectrum in terms of the flux of the planet divided by the flux of the star. The flux emergent from the entire disk of the planet is calculated using a four-point gaussian quadrature. The stellar flux is derived from a PHOENIX model (Hauschildt et al. 1999; Allard et al. 2001) assuming $T_{\rm eff} = 3350$ K (Maness et al. 2007), although we should note that the latest determinations of the stellar effective temperature from von Braun et al. (2012) are somewhat hotter at $T_{\rm eff} = 3416 \pm 54$ K (see also Bean et al. 2006; Nettelmann et al. 2010; Southworth 2010).

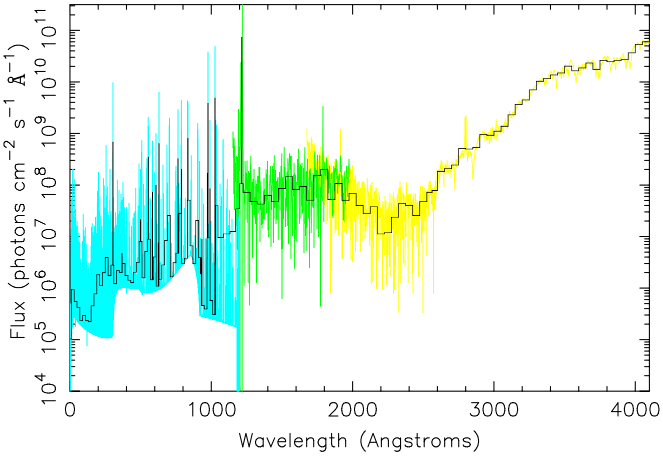

Figure 3. Adopted stellar ultraviolet spectrum for GJ 436 (black solid histograms) compared to NGSL spectra of GL 15B (yellow; see Heap & Lindler 2010), *IUE* spectra of GL 15B (green; Hubble MAST archive), and X-exoplanets theoretical spectra of GJ 436 (cyan; see Sanz-Forcada et al. 2011), all normalized to a distance of 1 AU.

(A color version of this figure is available in the online journal.)

3. RESULTS

Results from our chemical equilibrium and kinetics/transport models are presented below. We first investigate how the predicted equilibrium composition of generic hot Neptunes changes as a function of atmospheric temperature, metallicity, and C/O ratio. We discuss various interesting atmospheric compositional regimes that are not representative of planets in our own solar system, and we identify conditions for which CO rather than CH_4 is likely to be the dominant carbon component. We then focus on GJ 436b, determining whether the retrieval technique of Line et al. (2013) can shed any new light on the atmospheric composition of the planet, and we calculate disequilibrium chemical abundance profiles for several possible metallicities and thermal profiles. Finally, synthetic spectra from these disequilibrium models are compared with *Spitzer* transit and eclipse data, and observational consequences are discussed.

3.1. Chemical Equilibrium for Generic Hot Neptunes

With the core-accretion model of giant-planet formation (Mizuno et al. 1978; Bodenheimer & Pollack 1986; Pollack et al. 1996), a rocky or rock-ice protoplanetary core initially forms and grows from the accretion of solid planetesimals within a protoplanetary disk, with gaseous envelopes forming around these emerging protoplanets through core outgassing, direct accretion of nebular gas, and ablation of incoming solid planetesimals within the gaseous envelope. Rapid accretion of the surrounding largely H_2 and He nebular gas occurs when the protoplanet reaches a certain critical mass ($\sim 10\ M_\oplus$ in these traditional core-accretion models). The standard explanation for the "ice giants" Uranus and Neptune being so much more enriched in heavy elements than Jupiter and Saturn is that the accretion rate of solids was slow enough for the proto-Uranus and -Neptune that they did not completely reach the runaway gas-accretion-phase before the nebular gas was dispersed from the disk (e.g., Lissauer & Stevenson 2007). Elements heavier than hydrogen and helium therefore make up 80%–85% of Uranus and Neptune by mass (Podolak et al. 1995; Hubbard et al. 1995; Fortney & Nettelmann 2010). Depending on the degree of mixing between the core and atmosphere, the outermost gaseous envelope could have a heavy-element enrichment by mass ($Z_{\rm env}$) different from that of the bulk planet (e.g., Nettelmann et al. 2013); however, observations of CH_4 on the giant planets support the picture of a greater atmospheric $Z_{\rm env}$ for the ice giants Uranus and Neptune in comparison with the gas giants Jupiter and Saturn (e.g., Moses et al. 2004; Fouchet et al. 2009; Fegley et al. 1991; Gautier et al. 1995; Karkoschka & Tomasko 2009, 2011).

A metal-enriched atmospheric envelope might also be true for hot-Neptune exoplanets, despite potentially widely different evolutionary and migration histories. Although the hot Neptunes for which we have good constraints on both mass and radius show a large scatter in the mass-versus-radius relation, indicating likely different compositions, Weiss et al. (2013) demonstrate that there is a general trend toward increasing density with decreasing mass for planetary masses below $\sim 150\ M_\oplus$ (see also Miller & Fortney 2011). This trend suggests that smaller planets become progressively more enriched in heavy elements, similar to the situation in our own solar system. Planet-formation and population-synthesis models (e.g., Alibert et al. 2005; Figueira et al. 2009; Mordasini et al. 2012a, 2012b) also reflect this trend, with Fortney et al. (2013) predicting a significant increase in $Z_{\rm env}$ of Neptune-mass planets in comparison with planets more massive than $\sim 100\ M_\oplus$. There is also the possibility of in situ formation and capture of gas at small radial distances (e.g., Hansen & Murray 2012), which can lead to a variety of bulk gas fractions depending on planetary size and orbital distance.

To predict the atmospheric composition of any particular hot Neptune, we would need to know the properties of the protoplanetary disk in which the planet formed, the formation location within the disk, the planet's migration and impact history, and the details of the subsequent atmospheric evolution (e.g., interior outgassing, atmospheric escape, impact delivery/erosion, irradiation history, tidal heating, climate evolution, magnetospheric interactions, disequilibrium chemistry, etc.). Given the stochastic nature of some of these evolutionary processes and a lack of information about others, the task of predicting any particular atmospheric composition is exceedingly difficult (although the attempt can still be made, e.g., Alibert et al. 2006; Mousis et al. 2011; Madhusudhan et al. 2011b; moreover, population-synthesis models along the lines of those mentioned above can provide valuable insights into atmospheric properties of the ensemble). Instead of pursuing these types of models, we go through the simple exercise of investigating the expected equilibrium composition of Neptune-class exoplanets as a function of temperature, bulk metallicity, and bulk elemental ratios in the atmosphere. The increase in metallicity in these calculations then becomes a proxy for the evolution of smaller Neptune-mass planets, which are more likely to have high $Z_{\rm env}$ due to either inefficient gas accretion or efficient hydrogen escape.

Figure 4 illustrates how the atmospheric composition is expected to change as a function of either the atmospheric metallicity or the atmospheric C/O ratio for a few different temperatures at a pressure of 100 mbar. The 100 mbar pressure was selected here because it represents a typical infrared photospheric emission region in transiting-planet atmospheres. For these calculations, we use the protosolar abundances of Lodders et al. (2009) and assume an increase in metallicity occurs uniformly for all species except H, He, and Ne; moreover, we define the oxygen abundance through the C/O ratio, so the "metallicity" in this context refers to the C/H ratio (or X/H ratio, where X is any species except H, He, Ne, or O). This "C/H metallicity" should not be confused with bulk atmospheric metallicity, as the overall heavy-element enrichment will change with the C/O ratio—at very low C/O ratios, for example, the overall atmospheric metallicity, as defined by the abundance of C + O + all heavy elements in relation to that of the Sun, can be quite a bit higher than the C/H metallicity due to the exaggerated importance of the enhanced O. Condensates are not assumed to rain out in this equilibrium model. Given such simplifications and given that solar ratios of elements may not be preserved as a planetary atmosphere forms and evolves, the relevance of these calculations to real planets is questionable, but the exercise does effectively demonstrate that the atmospheric composition of hot Neptunes could be highly variable with atmospheric properties.

Exo-Neptunes with solar-like elemental ratios and moderately low metallicities could have hydrogen-dominated atmospheres very reminiscent of our own Neptune, but water and methane will make up an increasing fraction of the atmosphere with increasing metallicity, until H_2 itself becomes less important. At high-enough metallicities, exo-Neptunes can have CO_2-dominated atmospheres, qualitatively reminiscent of Venus. Carbon monoxide becomes an increasingly important constituent at higher temperatures and higher metallicities, and even O_2 can become dominant in equilibrium at very high metallicities and very low C/O ratios, further emphasizing that O_2 by itself is not necessarily a good indicator of biological activity on exoplanets (e.g., see Selsis et al. 2002; Segura et al. 2007; Schaefer et al. 2012; Hu et al. 2012).

These scenarios are borne out more clearly in Figure 5, which shows how the equilibrium abundances of several atmospheric species vary as a function of temperature and metallicity for an assumed pressure of 100 mbar and an assumed C/O ratio that is maintained at the protosolar value (C/O = 0.46) with an increase in metallicity (i.e., all elements except H, He,

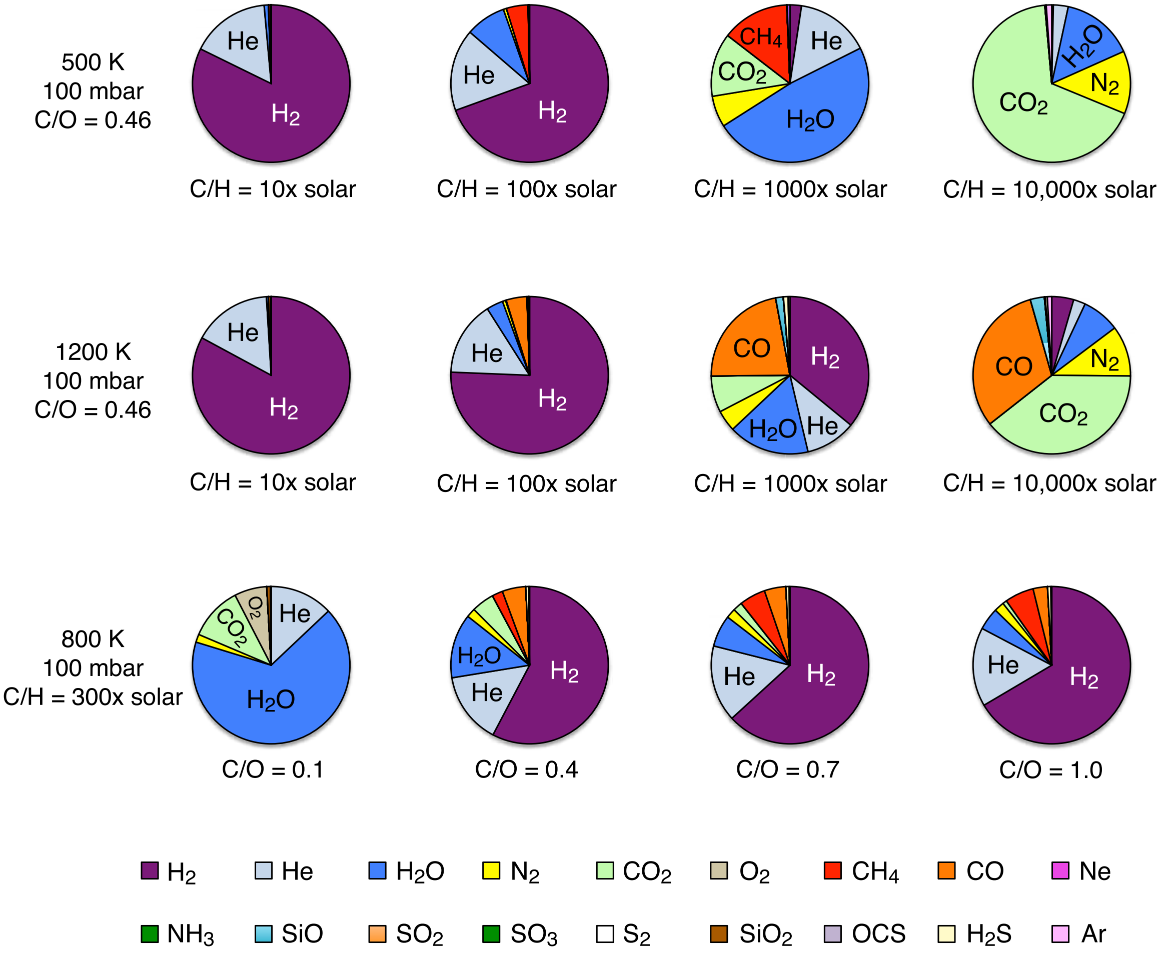

Figure 4. Pie charts illustrating equilibrium gas-phase compositions on generic hot Neptunes for different assumptions about atmospheric properties. The top row shows variations as a function of metallicity (10–10,000 times solar, as labeled) for an atmosphere with a solar C/O ratio, a pressure of 100 mbar, and a temperature of 500 K. The middle row is similar to the top row, except the assumed temperature is 1200 K. The bottom row shows variations as a function of the C/O ratio for an assumed metallicity of 300 times solar (i.e., protosolar abundances of all species except H, He, Ne, and O are multiplied by 300, with O being defined through the C/O ratio), a pressure of 100 mbar, and a temperature of 800 K. Note the very large variation in composition for different bulk atmospheric properties.

(A color version of this figure is available in the online journal.)

and Ne are increased by a constant factor). Because we do not have a complete set of condensates in these equilibrium calculations (and in particular, we are missing several Ca–Ti–Al silicates, see Lodders 2010), these gas-phase mixing ratios are not completely accurate, but the general trends with temperature and metallicity hold true. For example, Figure 5 demonstrates that H_2 becomes relatively less abundant at all temperatures as the metallicity is increased, whereas the water (H_2O) mole fraction increases roughly linearly with increasing metallicity at most temperatures, until H_2O starts to decrease at very high metallicities (e.g., $\gtrsim$1000 times solar) due to the overall decrease in the bulk H fraction. Methane (CH_4) is more stable at low temperatures, where its abundance also increases with increasing metallicity until the bulk hydrogen abundance drops and makes less H available to form methane. Carbon monoxide (CO) becomes more stable at high temperatures and high metallicities, where it is a significant atmospheric component under these conditions. Carbon dioxide (CO_2) is not very abundant at low metallicities, especially at low temperatures, but CO_2 increases significantly with increasing metallicity, becoming the dominant constituent at very high metallicities for all temperatures. Carbonyl sulfide (OCS) has a behavior similar to CO_2, although it is never as abundant. Solid graphite is stable in the lower-right corner of these plots in Figure 5 (high metallicities, low temperatures) and sequesters a notable fraction of the available carbon, thereby lowering the gas-phase C/O ratio in this region of temperature–metallicity space. Ammonia (NH_3) is abundant in equilibrium at the lowest temperatures considered, but N_2 becomes the most abundant nitrogen component at all temperatures as the metallicity is increased, although it never dominates the overall atmospheric composition at the conditions considered, assuming no further atmospheric evolution. The abundance of hydrogen cyanide (HCN; not shown in Figure 5) never rivals that of N_2 and NH_3, although its abundance increases with increasing temperature at moderately high metallicities. Hydrogen sulfide (H_2S) is the dominant sulfur constituent under the considered conditions, increasingly roughly linearly with metallicity until hydrogen becomes scarce.

Note that atmospheric metallicities of 10, 100, 1000, and 10,000 times solar correspond to $Z_{\mathrm{env}} = 0.13$, 0.61, 0.94, and 0.99, respectively, for solar ratios of the full suite of elements considered in the models (see Section 2.1). This range of Z_{env} variation is expected for Neptune-sized planets in the population-synthesis formation and evolution models of Fortney et al. (2013), with $Z_{\mathrm{env}} = 0.6$–0.9 being the most

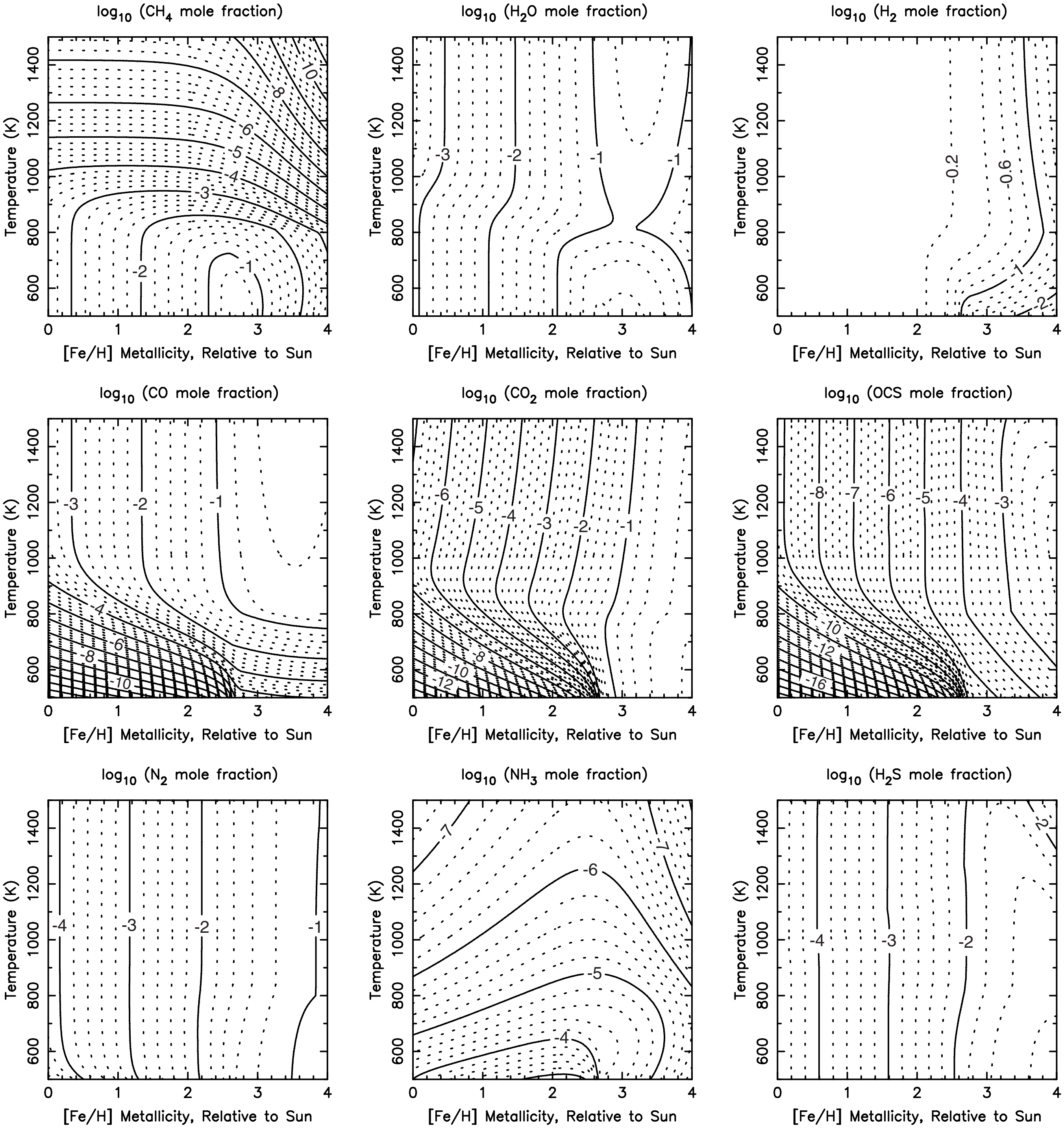

Figure 5. Equilibrium mole fractions for different gas-phase species as a function of temperature and metallicity for a solar ratio of elements (except H, He, and Ne remain solar at all metallicities), at a pressure of 100 mbar. When we present a metallicity [X/H] in square brackets here and in subsequent figures, we use the standard logarithmic definition; e.g., a metallicity of [Fe/H] = 3 corresponds to a heavy element enrichment of 1000 times solar.

common for such planets. We might therefore expect the whole range of possible phase space in Figure 5 to be represented in the hot-Neptune exoplanet population. Although Uranus and Neptune are good examples of the cool, moderate-metallicity, H_2-dominated end members, many hot-Neptune exoplanets would have atmospheric compositions that are not found in our own solar system, with various H_2O-, CO-, or CO_2-rich possibilities being particularly worth mentioning. We should also note that metallicities $\gtrsim$500–600× solar are not possible if the "metals" are brought in predominantly via water or very water-rich volatiles (and/or through H-rich species such as CH_4, NH_3, and H_2S)—assuming no further atmospheric evolution due to hydrogen escape or other fractionation processes—because such volatiles would also deliver large amounts of hydrogen to the atmosphere (Nettelmann et al. 2011).

Aside from bulk metallicity, the atmospheric composition is also dependent on the C/O ratio (Lodders & Fegley 1997; Seager et al. 2005; Kuchner & Seager 2005; Lodders 2010; Line et al. 2010; Madhusudhan et al. 2011a; Madhusudhan 2012; Kopparapu et al. 2012; Moses et al. 2013). It is unclear what

C/O ratio to expect for hot Neptunes, as that will depend greatly on the planet's original formation location (especially in relation to specific condensation fronts in the protoplanetary disk), as well as to its evolutionary history (e.g., Moses et al. 2013, and references therein). Atmospheric C/O ratios < 0.1 could occur if the disk or feeding zones were oxygen-rich or if planetesimals composed largely of water ice or clathrate hydrates dominated the delivery of heavy elements to the protoplanetary envelope. Similarly, the bulk C/O ratio could conceivably be greater than unity on giant planets (e.g., Lodders 2004; Madhusudhan et al. 2011a, 2011b; Madhusudhan 2012; Öberg et al. 2011; Mousis et al. 2012; Kopparapu et al. 2012; Moses et al. 2013) if the planet accreted carbon-rich solids inward of the water-ice line in the disk; if the planet accreted CO-rich, H_2O-poor gas from a region between the H_2O and CO ice lines, from a region in the innermost disk, or from within a heterogeneous disk or water-poor feeding zones; or if the disk were carbon-rich in the first place. However, graphite condensation followed by gravitational settling of the condensates (i.e., precipitation or "rain out") is expected to deplete the gaseous carbon and maintain the gas-phase C/O ratio near 1 above any graphite clouds in solar-metallicity exoplanet atmospheres (Lodders & Fegley 1997; Seager et al. 2005; Moses et al. 2013); therefore, we do not consider C/O ratios >1 in our current models. If the planet were so hot that graphite never becomes stable, if the graphite clouds were located within the photosphere, or if the graphite clouds were kinetically inhibited from forming even under conditions of thermodynamic-equilibrium stability, then photospheric gas-phase C/O ratios >1 would be possible (see Section 5 for more discussion).

In Figure 6, we show how the equilibrium abundances of several atmospheric constituents vary as a function of temperature and C/O ratio for an assumed 100 mbar pressure and a moderately high assumed C/H metallicity of 300 times solar (i.e., where all elements other than H, He, Ne, and O are assumed to be 300 times the protosolar abundances of Lodders et al. 2009). Recall here that we define the oxygen abundance through the C/O ratio, such that the very low C/O ratios at the left edge of these plots also correspond to large overall atmospheric metallicities, in addition to O being a dominant element. For example, our nominal solar C/H ratio is 2.78×10^{-4} and O/H ratio is 6.06×10^{-4}. For a uniform enrichment of all elements of 300 times solar, the corresponding C/H and O/H ratios would be 8.33×10^{-2} and 1.82×10^{-1}, respectively. For a C/H ratio of 300 times solar but oxygen defined via the C/O ratio from $\mathrm{O/H} = (\mathrm{C/H})/(\mathrm{C/O})$, a C/O ratio of 0.08 would correspond to an O/H ratio of 1.04, which is ∼1700 times the solar O/H ratio. Under such very low C/O ratio conditions (i.e., $\mathrm{C/O} \lesssim 0.08$) in this otherwise 300 times solar case, hydrogen is no longer the dominant element, and the H_2 abundance drops precipitously, as seen in Figure 6. Molecular oxygen then becomes the dominant gas at $\mathrm{C/O} \lesssim 0.04$ in this scenario—if such conditions have any relevance to real atmospheres—but H_2O quickly takes over with increasing C/O ratio to dominate at $0.05 \lesssim \mathrm{C/O} \lesssim 0.19$ (or at even greater C/O ratios for lower temperatures), whereas H_2 dominates at moderate-to-high C/O ratios ($\mathrm{C/O} \gtrsim 0.2$). Carbon monoxide becomes an important constituent at moderate-to-high temperatures and moderate-to-high C/O ratios, CH_4 and NH_3 are important at low temperatures for all but the lowest C/O ratios, and CO_2 is important under most conditions except for the lowest temperatures considered at high C/O ratios. HCN increases in significance at high temperatures and high C/O ratios. Molecular nitrogen (not shown in Figure 6) is relatively unaffected by the atmospheric C/O ratio. Condensed graphite is stable above ∼750 K for the higher C/O ratios.

Note the major and sudden shift from a more oxidized to a more reduced atmosphere at $\mathrm{C/O} \approx 0.7$ at high temperatures in Figure 6 for this 300 times solar-metallicity model. Graphite becomes stable at $\mathrm{C/O} \gtrsim 0.7$ as this shift occurs, methane and HCN become more prevalent, and water and CO_2 become less prevalent. This transition is equivalent to the one that occurs at C/O ratios near 1.0 for a solar-composition, solar-metallicity gas, as discussed extensively by Lodders & Fegley (1997), Madhusudhan (2012), and Moses et al. (2013). For any given pressure in the planet's photospheric region, this key transition occurs at lower C/O ratios for higher metallicities. Thus the transition to the Madhusudhan (2012) "carbon-rich" C2 class would occur at lower C/O ratios for higher-metallicity planets, and metallicity can be an additional complication for any composition-based classification scheme.

The phase boundaries and stability regimes for the dominant carbon-bearing gases under the conditions plotted in Figures 5 and 6 are further illustrated in Figure 7. The conditions under which graphite is stable are also shown (see Section 5 for additional discussion). Note that carbon dioxide dominates at very high metallicities and/or very low C/O ratios. At more moderate metallicities and C/O ratios, CH_4 dominates at low temperatures and CO at high temperatures.

The chemical-equilibrium results are also sensitive to pressure, as is shown in Lodders & Fegley (2002) and Visscher et al. (2006), for example. However, given that transport-induced quenching will affect the predicted abundances as a function of pressure in real atmospheres, we have simply chosen a single representative photospheric pressure for the above figures. The quench level may occur at higher pressures (lower altitudes) in hot-Neptune atmospheres, thereby affecting the predicted compositions, and the infrared photosphere of high-metallicity exoplanets may reside at lower pressures than our nominal choice of 100 mbar. In fact, we emphasize that these simple equilibrium models are largely phenomenological and are not designed to represent all the complex processes that have gone into shaping the atmospheric composition of actual exoplanet atmospheres. These equilibrium models do serve a useful purpose, though, in illustrating the possible diversity of hot Neptunes and in highlighting specific trends such as the increasing dominance of CO_2 at very high metallicities, the importance of H_2O at moderate-to-high metallicities for a variety of other conditions, and the change in the relative importance of methane and CO with increasing temperature. These general trends can be useful for considerations of the likely bulk atmospheric properties of specific hot Neptunes such as GJ 436b, based on the compositional clues provided by transit and eclipse data.

3.2. CHIMERA Retrieval Methods Applied to GJ436b

The secondary-eclipse data for GJ 436b (Stevenson et al. 2010; see also Beaulieu et al. 2011; Knutson et al. 2011; Stevenson et al. 2012) provide important constraints for compositional models. Madhusudhan & Seager (2011) use a Markov Chain Monte Carlo (MCMC) method to help identify the range of parameter space allowed for GJ 436b from comparisons of synthetic emission spectra with the *Spitzer* photometric data. Consistent with the earlier conclusions of Stevenson et al. (2010), Madhusudhan & Seager (2011) find that plausible GJ 436b models require a low methane abundance (e.g., mole fractions of 10^{-6}–10^{-7}) and a large a CO abundance (mole

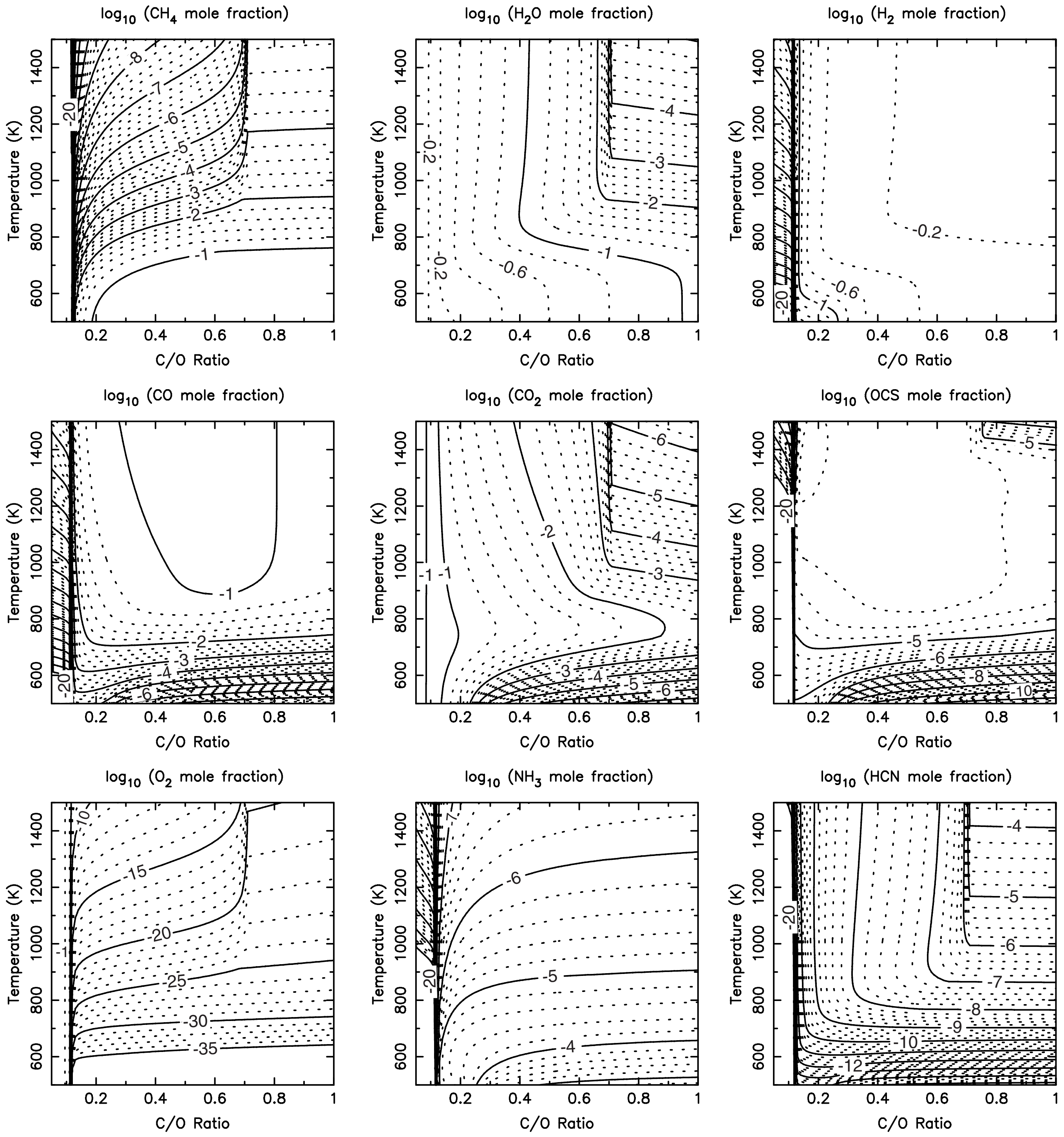

Figure 6. Equilibrium mole fractions for different gas-phase species as a function of temperature and C/O ratio for a 100 mbar pressure and a metallicity X/H = 300× solar (where X represents all elements except H, He, Ne, and O, with the O abundance being defined through the C/O ratio).

fraction $\geqslant 10^{-3}$), along with a H_2O mole fraction $\leqslant 10^{-4}$ and a CO_2 mole fraction in the range $\sim 10^{-6}$–10^{-4} in order to adequately reproduce the Stevenson et al. (2010) eclipse data. As is noted by Stevenson et al. (2010) and Madhusudhan & Seager (2011), such compositions are inconsistent with low-metallicity equilibrium models. Line et al. (2011) and Venot et al. (2013) further demonstrate that disequilibrium chemical processes like photochemistry and transport-induced quenching do not help resolve this problem.

The relatively sparse spectral coverage, low signal-to-noise ratio, and systematic uncertainties of the *Spitzer* secondary-eclipse data from GJ 436b and other exoplanets make retrieving atmospheric information difficult, as many solutions are statistically valid (Madhusudhan & Seager 2009, 2011; Lee et al. 2012; Line et al. 2012, 2013; Benneke & Seager 2012; Barstow et al. 2013). As a check on the derived best-fit abundances and thermal profile for GJ 436b, we apply the CHIMERA retrieval code of Line et al. (2013) to the Stevenson et al. (2010) secondary-eclipse data. Briefly, CHIMERA employs a suite of Bayesian retrieval algorithms—optimal estimation, bootstrap Monte Carlo, and differential-evolution MCMC—to determine the allowed range of temperatures and gas-phase mixing ratios

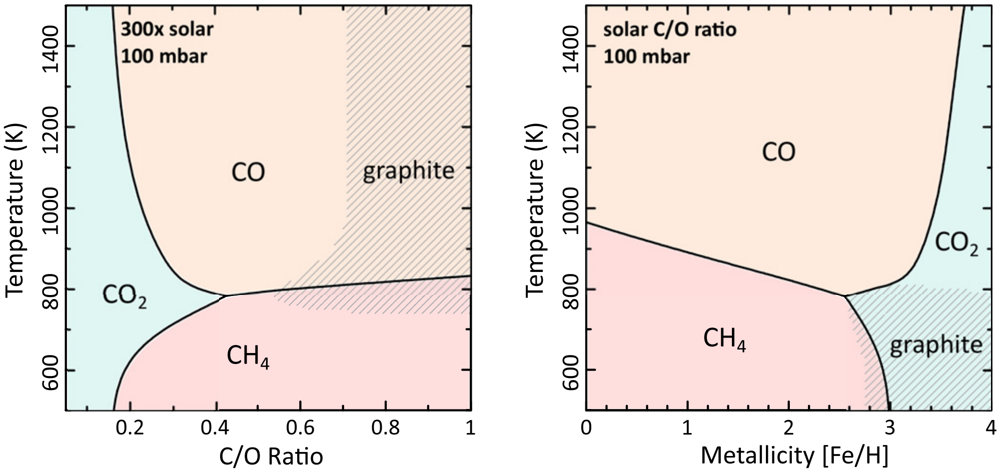

Figure 7. Dominant stability regimes in chemical equilibrium at 100 mbar for gas-phase carbon species as a function of temperature and bulk C/O ratio for 300 times solar metallicity (left) and as a function of temperature and metallicity for a solar C/O ratio (right). Conditions where graphite is stable are shaded.

(A color version of this figure is available in the online journal.)

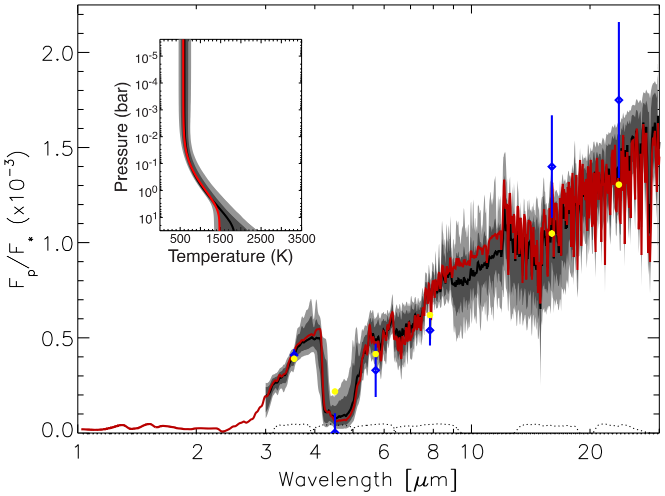

Figure 8. Synthetic emission spectra (flux of the planet divided by flux of the star) and thermal profile (insert) for GJ 436b derived from the differential-evolution Markov Chain Monte Carlo retrieval method described by Line et al. (2013). The span of solutions that fit within 2σ (light gray) and 1σ (dark gray) are shown in both the temperature-profile and spectral plots, along with the median of the ensemble of fits (black curves). The red curves in both plots represent a single best-fit model. The blue diamonds with error bars are the *Spitzer* secondary-eclipse photometric data from Stevenson et al. (2010), and the yellow circles show the best-fit model results convolved over the *Spitzer* bandpasses (with the bandpass sensitivities being plotted as dotted curves near the bottom of the plot).

(A color version of this figure is available in the online journal.)

for GJ 436b. Here we discuss the results of the differential-evolution MCMC approach. With this technique, the posterior probability distribution for each of the parameters that controls the temperature structure (based on the analytic parameterizations of Guillot 2010) and assumed constant-with-altitude mole fractions for H_2O, CH_4, CO, and CO_2 is characterized using a genetic algorithm that generates $\sim10^5$ models (see Line et al. 2013, for further details). The statistics from the retrieval are shown in Figures 8–10.

First, Figure 8 shows both the retrieved thermal structure and the corresponding spectra for the ensemble of models for GJ 436b generated from the differential-evolution MCMC approach. Rather than plotting the many thousands of spectra and thermal profiles generated from this retrieval approach, we instead plot the median of the spectra (or temperatures in the plot insert) in black, along with the 1σ and 2σ spread in the spectra (or temperatures) in dark gray and light gray, respectively. In essence, these spreads reflect the fact that if we were to draw a random set of parameters from the posterior probability distributions, there would be a 95% chance that the flux at any one wavelength corresponding to the *Spitzer* bandpasses would fall within the 2σ spread, and so on. Note that although the synthetic spectra qualitatively reproduce the 3.6 to 4.5 μm flux ratio from the *Spitzer* photometric data, the non-detection of the eclipse in the 4.5 μm bandpass is particularly difficult to reproduce (see also Stevenson et al. 2010; Madhusudhan & Seager 2011).

Next, Figure 9 shows histograms of the H_2O, CH_4, CO, and CO_2 mole fractions for GJ 436b from the marginalized posterior probability distribution, as derived from the differential-evolution MCMC approach. These distributions show that H_2O and CO are relatively well constrained from the GJ 436b secondary-eclipse spectra, with the most probable H_2O mole fraction residing within the range of a few times 10^{-7} to a few times 10^{-4}, and the most probable CO mole fraction restricted to $\gtrsim10^{-4}$, although the solutions for both H_2O and CO contain an extended, highly unconstrained tail at lower mixing ratios. The methane distribution also shows that the CH_4 mole fraction is restricted to values less than 10^{-6}. These results are consistent with the analysis of Madhusudhan & Seager (2011). The posterior CO_2 distribution has an interesting double-peaked structure that makes the precise value for the CO_2 mole fraction less well constrained, but viable solutions are found for mole fractions between 10^{-8} and 10^{-2}. This result for CO_2 is also consistent with the $\chi^2/N_{\rm obs} \leqslant 2$ results of Madhusudhan & Seager (2011), where $N_{\rm obs}$ is the number of available photometric data points. Our results confirm the picture of a GJ 436b atmosphere that possesses a large CO abundance, a very low methane abundance, and a moderately low water abundance.

Finally, Figure 10 shows the correlations in the retrieved abundances amongst the different gases. The CH_4 abundance remains low, regardless of the abundance of the other species, and thus the CH_4 mole fraction appears uncorrelated with either CO,

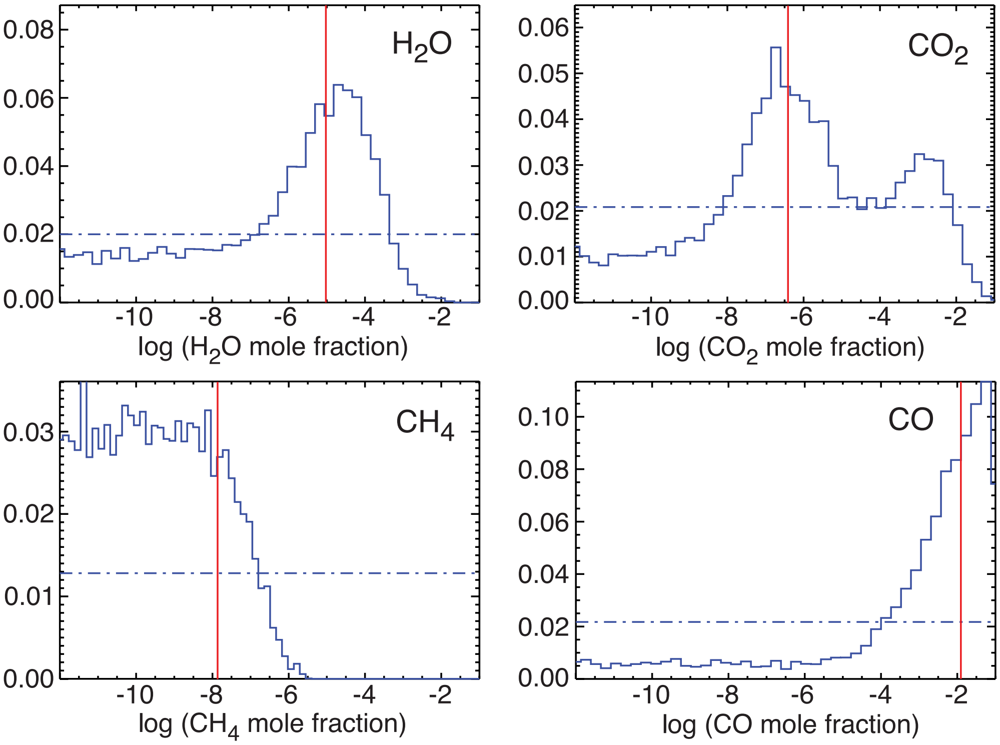

Figure 9. Gas mole-fraction histograms of the marginalized posterior probability distribution derived from the differential-evolution Markov Chain Monte Carlo retrieval approach (Line et al. 2013), as applied to the GJ 436b *Spitzer* eclipse data of Stevenson et al. (2010). The horizontal dot-dashed blue curves represent the priors, which are assumed to be flat (uninformative). The vertical red lines represent the mole fractions that correspond to the best-fit solution.

(A color version of this figure is available in the online journal.)

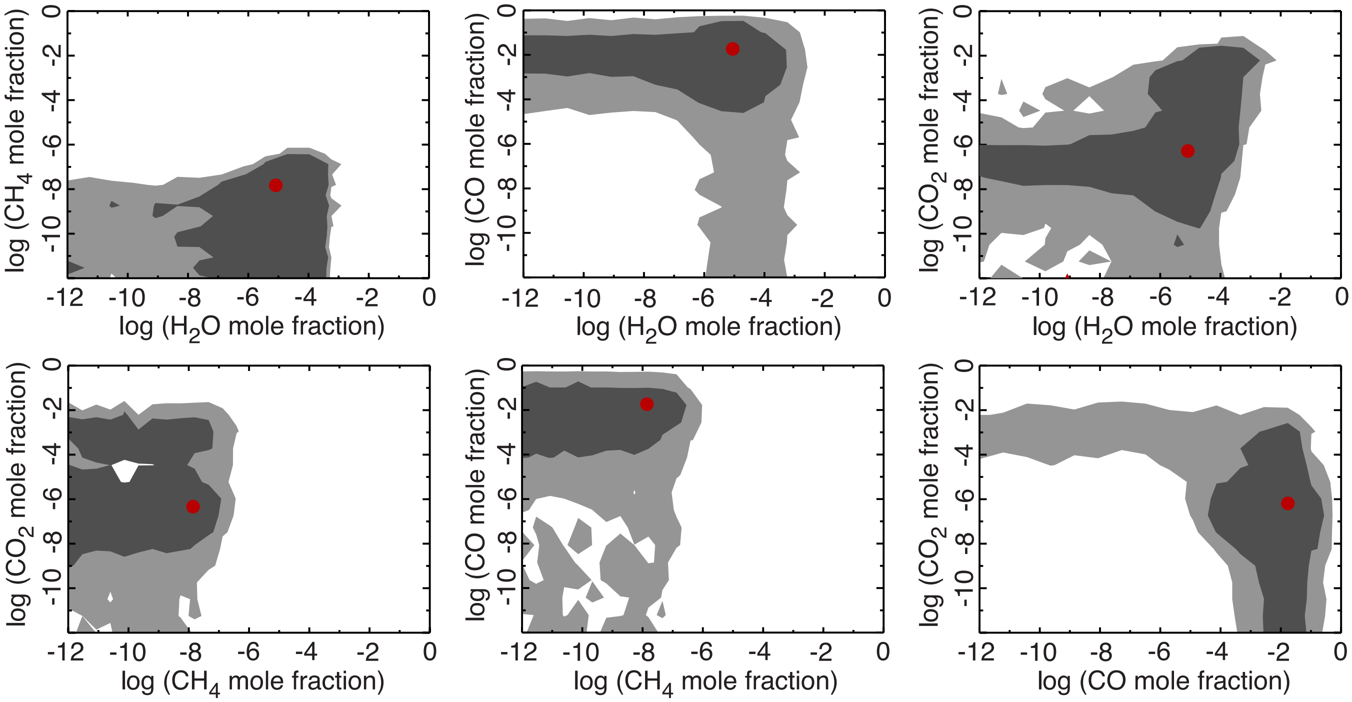

Figure 10. Contours of the gas-abundance constraints for GJ 436b derived from the differential-evolution MCMC posterior probability distributions, illustrating the correlations between the different gases. The dark gray regions represent the 1σ confidence interval and light gray regions represent the 2σ confidence interval. The red dot in each plot is the best-fit (maximum-likelihood) solution from the ensemble of 10^5 fits.

(A color version of this figure is available in the online journal.)

CO_2, or H_2O. An apparent correlation between CO and CO_2 results from the very low flux (non-detection) in the 4.5 μm *Spitzer* channel where both CO and CO_2 absorb: if the CO mole fraction is large enough, the CO_2 mole fraction is relatively unconstrained and can be low, but if the CO mole fraction is small, the CO_2 mole fraction must be large in order to explain the very low 4.5 μm flux. Note also that solutions with low CO and high CO_2 do not fit the data as well as models with relatively high CO, perhaps because the high-CO_2 solutions end up with too much absorption in the 16 μm *Spitzer* channel. Figure 10 also illustrates a correlation between CO_2 and H_2O. If water is fairly abundant, the CO_2 abundance is not well constrained, but if the water abundance is low, the CO_2 abundance is more tightly constrained to fall within a mole-fraction range of $\sim 10^{-8}$–10^{-6}. At the highest water abundances, there is also a positive correlation between H_2O and CO_2 in that very high water abundances require very high CO_2 abundances. This may reflect a strong correlation between H_2O (as the gas that has the largest overall influence on the spectrum) and temperatures, in that a very large water abundance can only be accommodated through high temperatures, at which point more CO_2 is needed to keep the low flux at 4.5 μm. Given that more solutions are found for low-to-moderate water abundances, the low-abundance peak for CO_2 in Figure 9 dominates over the secondary high-CO_2-abundance peak.

These new retrievals do not help resolve the apparent puzzles with respect to atmospheric composition on GJ 436b. Recalling Figures 5 and 6, a very low methane abundance can occur in equilibrium at very high temperatures at low metallicities (i.e., $T \gtrsim 1200$ K in the photosphere, hotter than is likely for GJ 436b) or at more moderate temperatures when the C/O ratio is low or when the atmospheric metallicity is very high. However, under those conditions, the H_2O abundance is likely to be significantly larger than is indicated by all the retrievals (above, and Madhusudhan & Seager 2011). Similarly, the preference for high CO mole fractions in the retrievals suggests a high metallicity for GJ 436b, which again implies unacceptably large water (and potentially CO_2) abundances. In fact, looking at Figures 5 and 6, we need to emphasize that there are no equilibrium chemistry solutions—or even, as we will show below, no disequilibrium chemistry solutions—that fall within the favored temperature-abundance ranges indicated by the retrievals. This result illustrates one potential drawback of retrievals from sparse, noisy, systematics-prone data: the solutions may reproduce the data well but not make any physical sense. Going to higher metallicities does help in general in that the photosphere is both hotter and more likely to reside in the CO-dominated regime (see Figure 1), but a high water abundance is a necessary consequence of high metallicity, unless the metallicity is so large ($\gtrsim$10,000 times solar) that the atmosphere contains very little H. That solution, which corresponds to $Z_{\rm env} = 0.994$, (i.e., 0.6% H/He by mass), is unfortunately ruled out by GJ 436b's mass–radius combination, according to most interior models (cf. Adams et al. 2008; Baraffe et al. 2008; Figueira et al. 2009; Rogers & Seager 2010a; Nettelmann et al. 2010; Miller & Fortney 2011).

Figure 11 illustrates the possible C/O ratio versus metallicity phase space that can accommodate a low methane abundance on GJ 436b for the assumption of a moderately hot, high-altitude photosphere (e.g., assuming 900 K at 10 mbar), which may be relevant for a high-metallicity GJ 436b atmosphere. The shaded regions in this plot are consistent with the retrieved CH_4 mole fractions of $\lesssim 1$ ppm, which can occur at low atmospheric C/O ratios and/or high metallicities. Again, there are no equilibrium solutions within the shaded regions of Figure 11 that are entirely consistent with the retrievals, with the main problem being too much H_2O and too much CO_2. However, the atmosphere is not likely to be in equilibrium (Line et al. 2010; Moses 2013), and we use these constraints as a guide for our disequilibrium kinetics and transport models, in an attempt to find forward models with more physically meaningful atmospheric properties that can provide a reasonable fit to the GJ 436b *Spitzer* secondary-eclipse data.

3.3. Disequilibrium Chemistry Modeling of GJ 436b

Photochemistry and transport-induced quenching can affect the predicted photospheric abundances on extrasolar giant planets, resulting in mixing ratios that are often orders of magnitude different from chemical-equilibrium expectations (Liang et al. 2003, 2004; Zahnle et al. 2009; Line et al. 2010, 2011; Moses et al. 2011, 2013; Miller-Ricci Kempton et al. 2012; Kopparapu et al. 2012; Hu et al. 2012; Venot et al. 2012, 2013). Most disequilibrium models to date have focused either on giant planets with a near-solar-like complement of elements or on hydrogen-poor terrestrial exoplanets or super-Earths. We now test various scenarios with moderate and high metallicities (but still containing a non-negligible hydrogen mass fraction) for GJ 436b using disequilibrium kinetics/transport models to see how photochemistry and transport-induced quenching can alter the predicted transit and eclipse spectra. We start with the first-principles-based temperature profiles shown in Figure 1 and adopt a solar C/O ratio and a constant eddy diffusion coefficient of $K_{zz} = 10^9$ cm^2 s^{-1} for these initial models. Figure 12 shows how the model results for CH_4, H_2O, CO, and CO_2 compare with the mixing ratios retrieved from the *Spitzer* secondary-eclipse data. This figure demonstrates that even when photochemistry and transport-induced quenching are considered, none of these models can reproduce the abundances derived from the retrievals.

The mixing-ratio profiles for other potentially interesting species in these disequilibrium models are shown in Figure 13. The species profiles for the 1 times solar model are qualitatively similar to those of Line et al. (2011): behind H_2 and He, the next most abundant gases are H_2O, CH_4, and NH_3. Water survives at a near-equilibrium abundance until very high altitudes ($\sim$1 μbar), at which point photolysis and other destruction mechanisms start to irreversibly convert the H_2O to CO and other oxygen-bearing species. Although photolysis and other chemical mechanisms operate to destroy H_2O at lower altitudes, water is efficiently recycled in the background H_2 atmosphere, and H_2O remains the dominant infrared opacity source in these 1 times solar models. Methane is even less stable than water at high altitudes, due primarily to the large H abundance released by H_2O photolysis and subsequent catalytic destruction of H_2 (e.g., Liang et al. 2003; Moses et al. 2011). The carbon that was in high-altitude CH_4 gets photochemically converted to CO, C_2H_2, HCN, and atomic carbon, primarily (see Moses et al. 2011 for details). Ammonia is photolyzed by longer-wavelength UV radiation that can penetrate a bit deeper in the atmosphere, and the nitrogen liberated by the NH_3 photodestruction largely ends up as HCN and atomic N. There are some quantitative differences between our 1 times solar model and that of Line et al. (2011) due to different adopted reaction rate coefficients, K_{zz} assumptions, stellar ultraviolet flux, and atmospheric temperatures, but the results from both Line et al. (2011) and our own models indicate that CH_4 survives photochemical destruction throughout the bulk of the $\sim$0.0001–1 bar photosphere on the 1 times solar GJ 436b. As a result, the 1 times solar model has more methane than is indicated by the retrieval analyses of the *Spitzer* secondary-eclipse data (see Figure 12, Section 3.2, and Madhusudhan & Seager 2011).

The resulting spectrum for the 1 times solar model does not compare well with the *Spitzer* secondary-eclipse data (Figure 14). One obvious problem is a reversed 3.6 to 4.5 μm

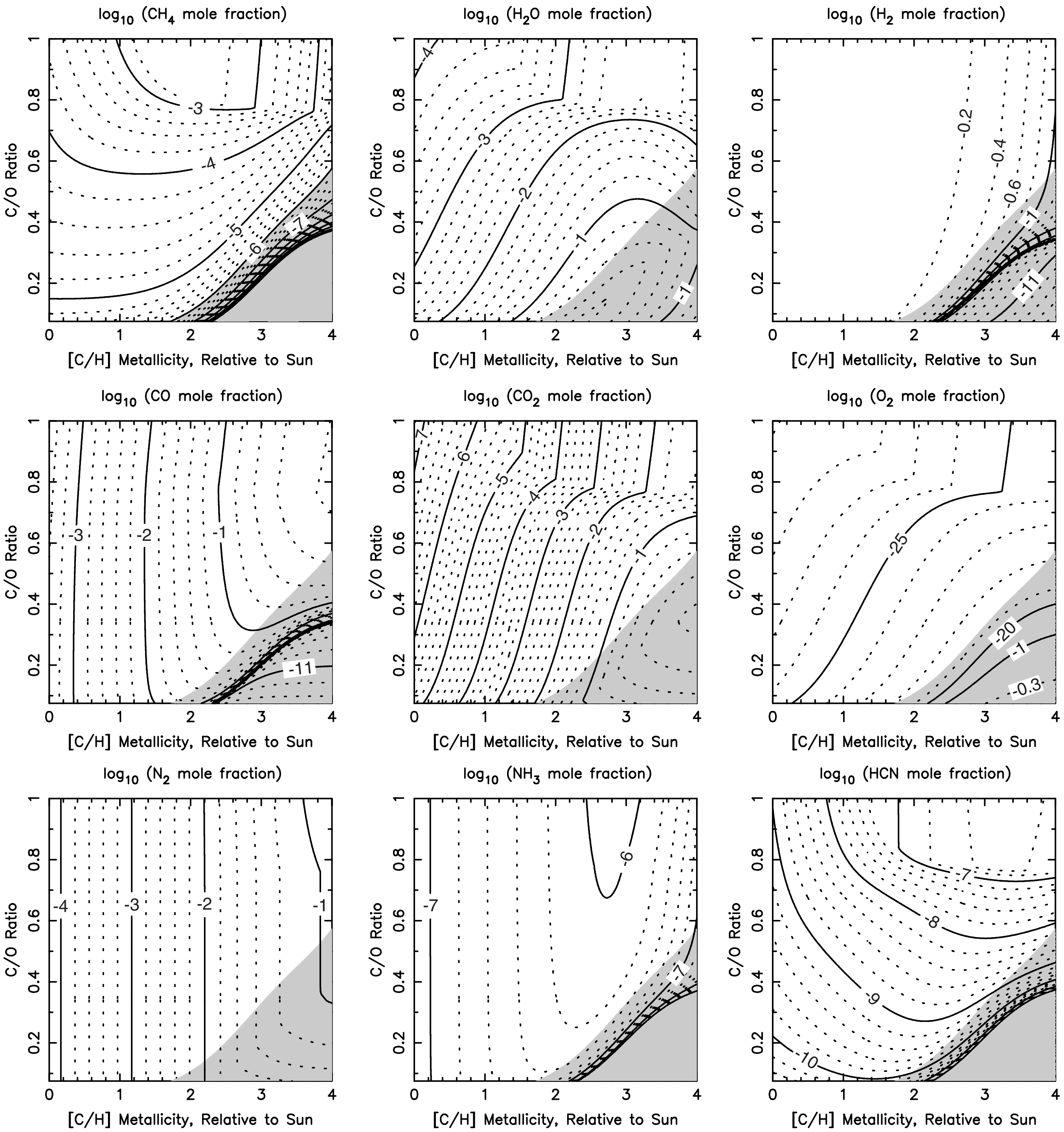

Figure 11. Equilibrium mole fractions for different species as a function of C/H metallicity (see text) and C/O ratio at 900 K and 10 mbar (i.e., a relatively hot, high-altitude photosphere, which may be relevant to a high-metallicity GJ 436b). The shaded region in each plot is where methane has a mole fraction below 10^{-6}, as is indicated by retrievals based on the Stevenson et al. (2010) *Spitzer* GJ 436b secondary-eclipse data (our work, and that of Madhusudhan & Seager 2011).

flux ratio in comparison with observations. The CO–CH_4 quench point in the 1 times solar model occurs within the CH_4-dominated regime, so that the quenched CO abundance is relatively small, and the methane abundance is large. Since the equilibrium abundance of CO is everywhere lower than that of CH_4 with the 1× solar thermal profile (see Figure 1), there is no eddy K_{zz} value we could adopt that would change this conclusion. Some CO is produced at high altitudes from CH_4 and H_2O photochemistry, but the CO column abundance is never large enough to influence the relative 3.6 to 4.5 μm flux ratio. The large methane abundance therefore results in a lower flux (more absorption) at 3.6 μm in comparison with 4.5 μm. Another obvious problem is the overall lower brightness temperature at most wavelengths in comparison with the data. The thermal profile from Lewis et al. (2010) adopted in the 1 times solar model is not significantly colder than the profiles derived from the thermal retrievals shown in Madhusudhan & Seager (2011) or in Section 3.2, but the 1 times solar model does have a water abundance at the upper end (or greater than) the retrievals indicate (see Figure 12). Water accounts for most of

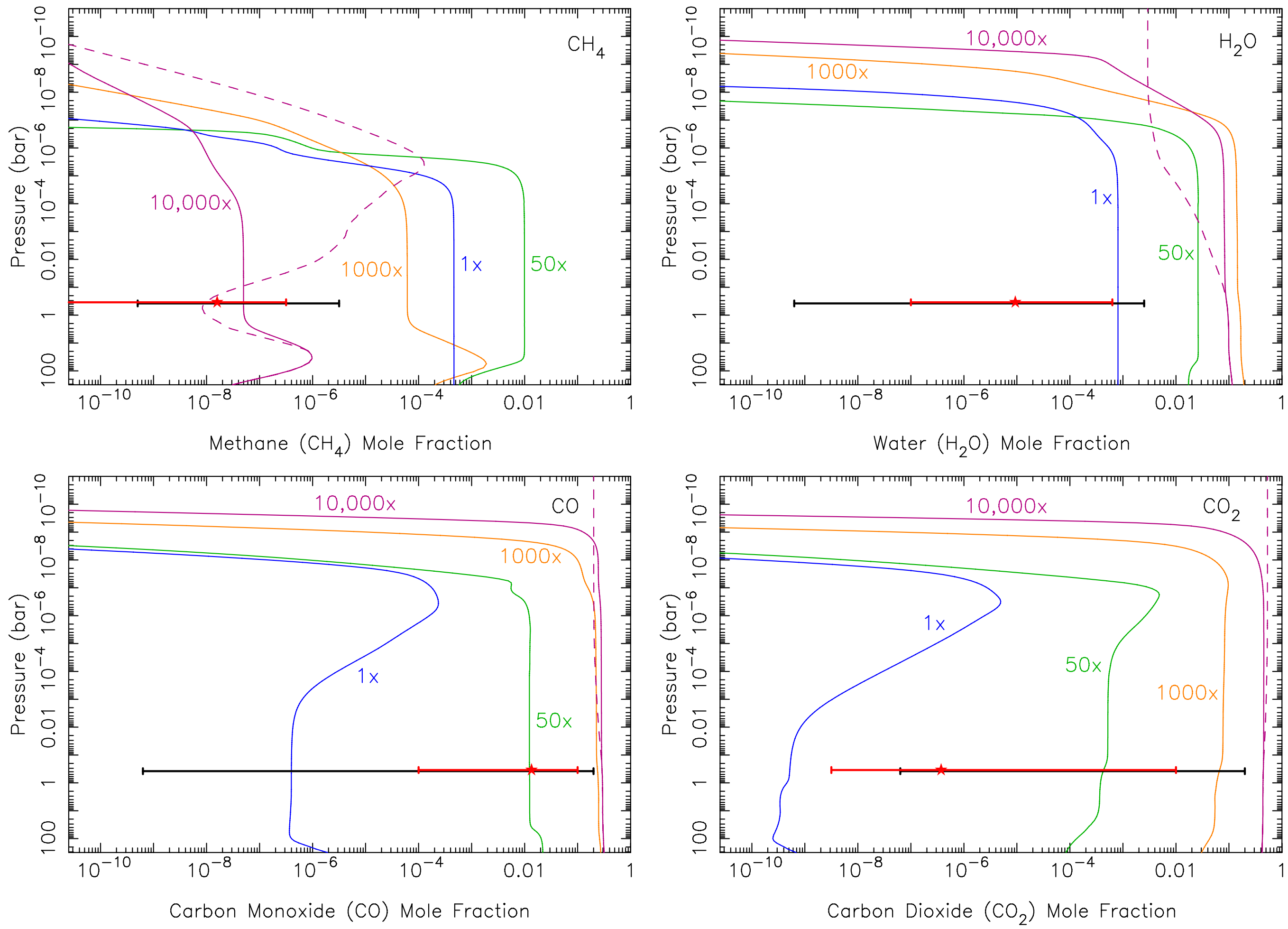

Figure 12. Mixing-ratio profiles for CH_4 (top left), H_2O (top right), CO (bottom left), and CO_2 (bottom right) from our kinetics/transport models for GJ 436b, for assumed atmospheric metallicities of 1 times solar (blue solid lines), 50 times solar (green solid lines), 1000 times solar (orange solid lines), and 10,000 times solar (purple solid lines), as described more fully in Figure 13. The corresponding equilibrium solutions for the 10,000 times solar model are shown as dashed purple lines. The red horizontal bar illustrates the most-probable solutions derived from the differential-evolution MCMC approach discussed in Section 3.2, with the star representing the best-fit solution. The black horizontal bar represents the model solutions from Madhusudhan & Seager (2011) that fit the *Spitzer* data to within $\chi^2/N_{\text{obs}} \leqslant 1$. Note that none of the disequilibrium models for the different metallicities have mole fractions that fall within the retrieval constraints for all four species.

(A color version of this figure is available in the online journal.)

the absorption in the 1 times solar model, and the relatively large water abundance leads to more absorption at most wavelengths than can be accommodated by the observations—hence the requirement of a low water abundance from the retrievals in the first place. Since photochemistry does not permanently destroy the photospheric water and methane in our 1 times solar models, such models cannot explain the *Spitzer* secondary-eclipse data.

The quench point for the 50 times solar model is closer to the equilibrium CO–CH_4 equal-abundance boundary due to an overall hotter atmosphere (see Figure 1), and both CO and CH_4 end up being major atmospheric constituents (see Figure 13). Carbon dioxide and molecular nitrogen also become more important constituents at the higher 50 times solar metallicity, while ammonia becomes relatively less important due to the N_2–NH_3 quench point falling within the N_2-dominated regime. Because NH_3 is more photochemically active than N_2, the photochemical production of HCN and complex nitriles does not increase significantly at high altitudes in the higher-metallicity model because the overall NH_3 mixing ratio has not changed much between 1 times and 50 times solar metallicities. However, the column abundance of HCN actually increases with the increased metallicity here because of thermochemical kinetics and the quenching of CH_4 and NH_3 at higher-than-equilibrium abundances (i.e., HCN in the photosphere maintains a pseudo-equilibrium with the quenched NH_3 and CH_4; see Moses et al. 2011, 2013). Carbon dioxide is produced effectively at high altitudes from the photochemistry of CO and H_2O, but equilibrium through the net reaction $CO + H_2O \leftrightarrows CO_2 + H_2$ is maintained kinetically through much of the photosphere. Although the CO mole fraction in the 50× solar model now falls within the range required by the retrievals discussion in Section 3.2, both H_2O and CH_4 are much more abundant than is allowed by the retrievals, and the 50× solar model does not fit the *Spitzer* secondary-eclipse data well.

At metallicities of 1000 times solar, hydrogen and helium now make up only ~6% of the atmosphere by mass. The methane abundance has dropped significantly in the 1000 times solar-metallicity model because the CH_4–CO quench point lies within the CO-dominated regime. The resulting CO/CH_4 ratio is finally in the right direction to explain the observed relative 3.6 to 4.5 μm flux ratio from the *Spitzer* eclipse data. Carbon monoxide begins to rival H_2 as the dominant constituent, and H_2O, CO_2, and N_2 are all very abundant. The atmosphere as a whole is more oxidized, and species like

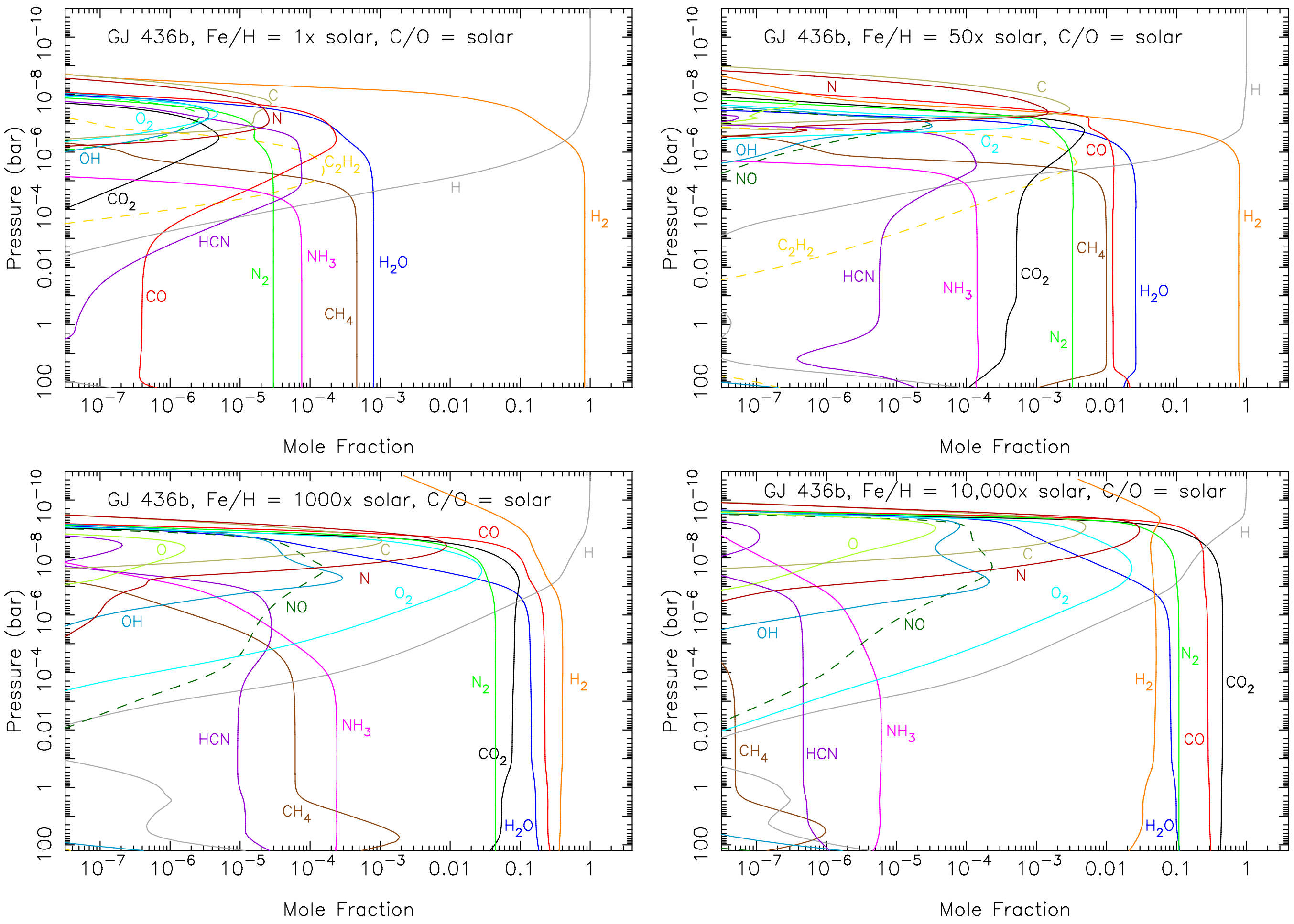

Figure 13. Mixing-ratio profiles for several species of interest (as labeled) in our kinetics/transport models for GJ 436b, for assumed atmospheric metallicities of 1 times solar (top left), 50× solar (top right), 1000 times solar (bottom left), and 10,000 times solar (bottom right). The thermal profiles adopted in these models are described in Section 2.2 (see Figure 1); the profile for the 10,000 times solar model (not shown in Figure 1) was derived from the PHOENIX model (Hauschildt et al. 1999; Allard et al. 2001; Barman et al. 2005) and is very similar to the 1000 times solar profile. The C/O ratio is assumed to be the protosolar value of Lodders et al. (2009) with 21% of the oxygen unavailable due to being bound up in condensates at deep atmospheric levels (Visscher et al. 2010a), and the eddy diffusion coefficient K_{zz} is assumed to be constant at 10^9 cm^2 s^{-1}.

(A color version of this figure is available in the online journal.)

O_2 and NO that are produced from photochemistry at high altitudes are able to survive more readily than they do in a more reducing atmosphere. The fact that elements other than O, C, N, and H have been neglected from these disequilibrium models (particularly Cl and S) will have an impact on the resulting abundances in these higher-metallicity models due to omitted catalytic cycles (e.g., Yung & DeMore 1999), and atmospheric escape and other evolutionary processes will likely alter this simple picture of steadily increasing metallicity, but the general supplantation of H_2 and the increasing dominance of CO_2 with increasing metallicity is a robust conclusion. At atmospheric metallicities of 10,000× solar, for instance, hydrogen and helium make up only ∼0.6% of the atmosphere by mass, and Figure 13 shows that CO_2 has solidly replaced H_2 as the dominant constituent, and even CO, N_2, and H_2O are more abundant than H_2.

Figure 14 shows that the 1000 times solar-metallicity model fares better in reproducing the *Spitzer* secondary-eclipse data than the 1 times solar-metallicity model did. The flux in the 3.6 μm channel is predicted to be greater than that in the 4.5 μm model now with the 1000 times solar model, due to the CH_4 abundance being much less than the CO abundance. The 1000 times solar model still provides too much absorption at 3.6 μm to be consistent with the eclipse depth as determined by Stevenson et al. (2010), indicating too much methane in the model; however, we should note that Beaulieu et al. (2011) derive both a lower 3.6 μm flux and a larger uncertainty in the eclipse depth at this wavelength (and at 4.5 μm), and the 1000× solar model more readily satisfies those constraints. More intriguing is the excellent fit in the 5.8 and 8.0 μm channels where water in this model is providing the dominant opacity source. This good fit with a water abundance that exceeds a 10% mixing ratio—in contrast to the much lower abundances derived from the retrievals—reflects the influence of the higher-temperature photosphere that results from the increased atmospheric opacity at high metallicities. The water abundance and photospheric temperatures are closely linked, and a hotter photosphere requires more water to remain consistent with the 5.8 and 8.0 μm eclipse depths, whereas, conversely, a colder photosphere requires less water. Still, this 1000 times solar model provides a relatively poor fit to the eclipse data of Stevenson et al. (2010, 2012), providing a $\chi^2/N_{\mathrm{obs}} \sim 11.5$, with the main problem being a 3.6 μm flux that is much lower than observed, but also a 4.5 μm flux that is in excess of the observational upper limit and a 16 μm flux that is much lower than observed (due to CO_2 absorption).

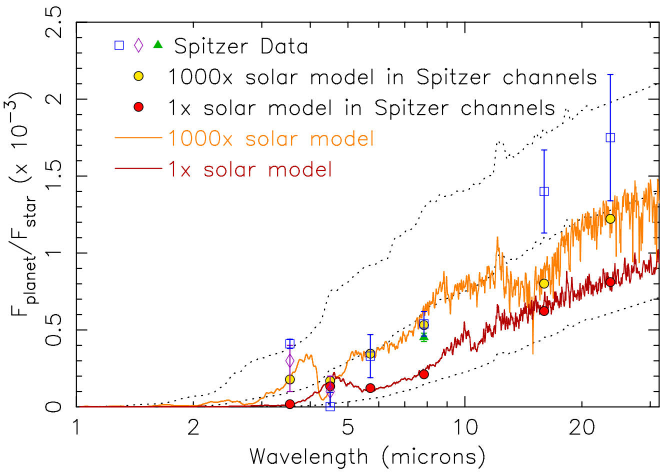

Figure 14. Synthetic emission spectra for GJ 436b for our disequilibrium models that assume a 1 times solar-metallicity atmosphere (dark red) and a 1000 times solar-metallicity atmosphere (orange), in comparison with observations (data points with error bars). The thermal profiles assumed in the models are shown in Figure 1, and the abundance profiles are shown in Figure 13. The blue squares represent the *Spitzer* secondary-eclipse data analyzed by Stevenson et al. (2010), with an updated upper limit at 4.5 μm from Stevenson et al. (2012), the purple diamonds represent the Beaulieu et al. (2011) analysis of the same 3.6 and 4.5 μm data, and the green triangle represents the analysis of 11 secondary eclipses of GJ 436b in the 8 μm channel by Knutson et al. (2011). The red and gold circles represent, respectively, the fluxes from the 1 times and 1000 times solar models, averaged over the *Spitzer* bandpasses. The black dotted lines represent the planetary emission (smoothed) assuming GJ 436b radiates as a blackbody at a temperature of 500 K (lower curve), 800 K (middle curve), or 1100 K (upper curve). The apparent emission "spikes" represent stellar absorption, as everything here is plotted in terms of the flux of the planet divided by the flux of the star. A PHOENIX stellar model (e.g., Hauschildt et al. 1999) with $T_{\rm eff} = 3350$ K was assumed for the host star for all these calculations.

(A color version of this figure is available in the online journal.)

Although the 1000 times solar-metallicity model itself does not provide a good fit to the Stevenson et al. (2010, 2012) secondary-eclipse data, and none of the models in Figure 12 fall within the constraints imposed by the retrievals for all the species, the model-data comparisons do suggest further avenues to explore with higher-metallicity models. The larger observed brightness temperature at 3.6 μm in relation to that at 5.8 and 8 μm in the *Spitzer* data suggests that the atmosphere has a sharper thermal gradient than the one derived from the 1D PHOENIX model, given that the contribution functions at the three wavelengths are not hugely separated in terms of the pressures at which they peak in the high-metallicity models. We note that both the dayside-average profiles from the 3D GCMs of Lewis et al. (2010) and the thermal profiles derived from the retrievals exhibit a larger thermal gradient in the relevant photospheric region than the 1000 times solar 1D PHOENIX models do. A larger thermal gradient could also result in a hotter atmosphere at the CH_4–CO quench point, if the quench point occurs at a high-enough altitude, pushing the atmosphere toward greater CO dominance at the expense of CH_4. That would improve the relative 3.6 to 4.5 μm flux ratio in comparison with observations. To investigate such a scenario, we simply scale one of the thermal profiles derived from the Madhusudhan & Seager (2011) MCMC analysis upward uniformly in altitude to lower pressures and run different disequilibrium chemistry models, assuming different bulk atmospheric properties. The results from one such model are shown in Figure 15.

For the model presented in this figure, the atmospheric C/H and N/H metallicity are assumed to be 300 times solar, the C/O ratio above the silicate clouds is assumed to be 0.6 (which actually requires a slightly sub-solar initial bulk C/O ratio if ∼21% of the oxygen is sequestered in silicates and other condensates at deeper atmospheric levels, as expected by Lodders 2010 and Visscher et al. 2010a), and the eddy diffusion coefficient follows the relation $K_{zz} = 10^7$ cm^2 s^{-1} at pressures $P \geqslant 10^{-4}$ bar, with K_{zz} increasing with the inverse square root of atmospheric pressure at $P < 10^{-4}$ bar. The thermal profile as shown in the insert of Figure 4 of Madhusudhan & Seager (2011) has been shifted upward uniformly by -1.2 in $\log_{10}(P)$ (i.e., pressures have been multiplied by $10^{-1.2}$) to account for the higher-altitude photosphere that will result from the higher metallicity. The 300 times solar atmospheric metallicity in this model is consistent with the interior models for GJ 436b (Adams et al. 2008; Baraffe et al. 2008; Figueira et al. 2009; Rogers & Seager 2010a; Nettelmann et al. 2010; Miller & Fortney 2011), and the lower value of K_{zz} in the lower atmosphere allows CH_4 to remain in equilibrium until ∼0.1 bar, at which point the methane quenches at the desired <1 ppm abundance. Judging from the PHOENIX models, the thermal profile at photospheric pressures may be hotter in this model than is expected on average in the dayside hemisphere of GJ 436b at this metallicity, so the likelihood of this scenario will need to be investigated by further 3D circulation modeling, but given that the observed emission will derive preferentially from the hottest regions on the observed disk, the profile does not appear to be unreasonably hot.

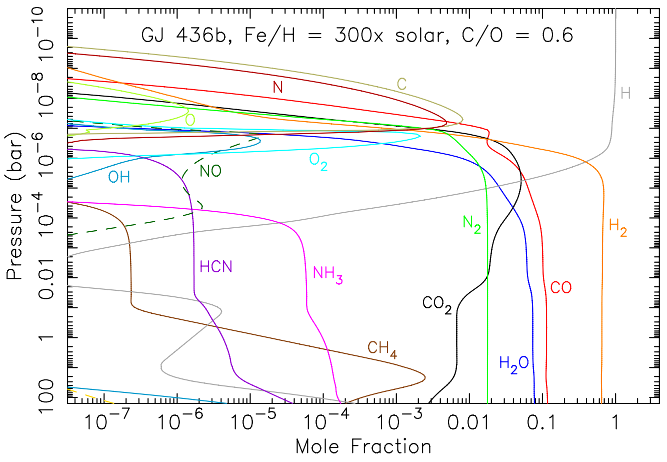

Figure 15. Mixing-ratio profiles for several species of interest (as labeled) in our kinetics/transport models for GJ 436b, for an assumed atmospheric metallicity of 300× solar in carbon and nitrogen, with the oxygen elemental abundance defined through an assumed C/O ratio of 0.6. The eddy diffusion coefficients are taken to be $K_{zz} = 10^7$ cm^2 s^{-1} at $P \geqslant 10^{-4}$ bar, with K_{zz} increasing as the inverse square root of the pressure at $P < 10^{-4}$ bar. The thermal profile is taken from Figure 4 of Madhusudhan & Seager (2011), but we have shifted the entire profile upward uniformly in an attempt to account for the higher-altitude photosphere with higher metallicities (see text).

(A color version of this figure is available in the online journal.)

Figure 15 shows that H_2 is still the dominant atmospheric constituent (by number) in the atmosphere in this 300 times solar-metallicity model, although both CO and H_2O at mole fractions of ∼10% each are encroaching on the H_2 dominance. Kinetic production of CO_2 from H_2O and CO occurs in the middle and upper photosphere in this model, allowing the CO_2 abundance to exceed that of water at high altitudes. Quenching of ammonia at non-negligible values occurs and is responsible for maintaining HCN at greater than ppm levels. The CH_4 abundance remains low, and the emission spectrum (Figure 16) is dominated by opacity from H_2O, CO_2, and CO. This model

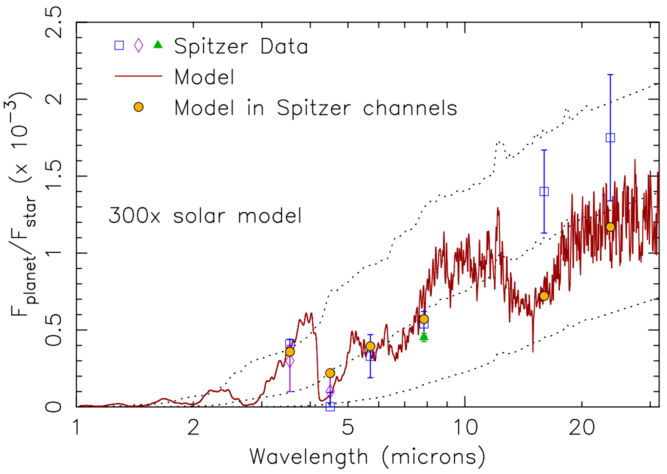

Figure 16. Synthetic emission spectra (dark red) for GJ 436b for our disequilibrium model that assumes a 300× solar-metallicity atmosphere, with a C/O ratio of 0.6 (see text and Figure 15). The blue squares represent the *Spitzer* secondary-eclipse data analyzed by Stevenson et al. (2010), with an updated upper limit at 4.5 μm from Stevenson et al. (2012), the purple diamonds represent the 3.6 and 4.5 μm *Spitzer* analysis of Beaulieu et al. (2011), and the green triangle represents additional *Spitzer* eclipse data at 8 μm as analyzed by Knutson et al. (2011). The red circles represent the model fluxes averaged over the *Spitzer* bandpasses. The black dotted lines represent the planetary emission assuming GJ 436b radiates as a blackbody at a temperature of 500 K (lower curve), 800 K (middle curve), or 1100 K (upper curve). See Figure 14 for further details.

(A color version of this figure is available in the online journal.)

finally has a low-enough methane abundance that the 3.6 μm flux from the *Spitzer* secondary-eclipse analysis of Stevenson et al. (2010) is better reproduced. The resulting 3.6 to 4.5 μm flux ratio is also more in line with observations, although this model, like all others including the retrievals, still produces too much flux in the 4.5 μm band. This result is more a function of the atmosphere being too hot where the contribution function peaks at 4.5 μm, rather than being due to insufficient CO and CO_2, as can be readily seen in Figures 12 and 15. In fact, the very large CO_2 abundance in this 300 times solar-metallicity model produces too much absorption in the 16 μm *Spitzer* channel, where the contribution function peaks at cooler, higher altitudes due to the large CO_2 column abundance. The non-detection of the GJ 436b secondary eclipse at 4.5 μm is difficult to explain by any known physically reasonable scenario without adversely affecting the fit at other wavelengths. In terms of the statistical fit to all the Stevenson et al. (2010, 2012) secondary-eclipse depths, this model fares better, at $\chi^2/N_{\rm obs} = 2.8$. The primary problems are insufficient flux at 3.6, 16, and 24 μm, and too much flux at 4.5 μm.

This particular forward model is not unique in terms of fitting the data, and there are numerous models with atmospheric metallicities in the couple-hundred to couple-thousand times solar range that fit the *Spitzer* data to within $\chi^2/N_{\rm obs} \leqslant 3$ (see, for example the 2000 times solar-metallicity model we presented in Richardson et al. 2013), but we have not found any disequilibrium chemistry models that fit to within $\chi^2/N_{\rm obs} \leqslant 2$. All of these high-metallicity models produce too much CO_2 to be consistent with the observed flux in the 16-μm channel. Models with high metallicities in the 100–10,000 times solar range also end up with a large water abundance, which then requires a hot photosphere to explain the 5.8, 8.0, and 24 μm fluxes, at which point there is too much emission at 4.5 μm. Slightly cooler models than the one shown in Figures 15 and 16 tend to fit better at 4.5 μm, but then the fit tends to be worse at 3.6 and 24 μm. Hotter models fit the 24 μm flux better, but then the fit at 4.5, 5.8, and 8.0 μm is worse. Going to a higher C/O ratio will help remove excess CO_2 to improve the fit at 16 μm, but then CH_4 becomes too abundant to explain the 3.6 μm flux. Lower C/O ratios help keep the methane abundance low, but then the problems with excess H_2O and CO_2 are exacerbated. Therefore, while these high-metallicity models are promising in their ability to qualitatively reproduce several aspects of the observed secondary-eclipse observations, several quantitative problems remain. The solutions derived from the retrieval methods (Section 3.2 and Madhusudhan & Seager 2011) provide a better overall fit to the data, but problems with the fit still remain at 4.5 and/or 16 μm; more importantly, these solutions have problems with plausibility in that it is difficult to theoretically explain how such abundances (e.g., the inferred CO/H_2O ratio) could be obtained chemically or physically in an atmosphere with any reasonable bulk properties. Therefore, despite the less-than-perfect fit to the existing GJ 436b secondary-eclipse data, such high-metallicity models should not be dismissed out of hand.

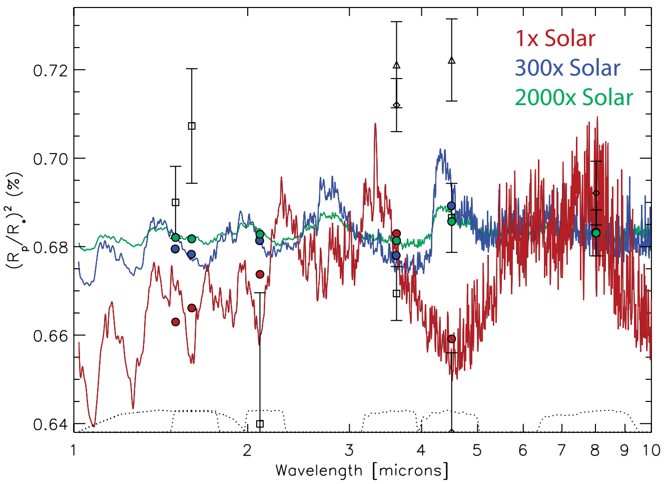

Figure 17. Synthetic transmission spectra for GJ 436b (in terms of the apparent transit depth, i.e., the square of the ratio of the planetary radius to the stellar radius) for our disequilibrium models that assume a 1 times (red), 300 times (blue), and 2000 times (green) solar metallicity. Scattering from molecules or hazes is not included in the calculations. Data points from various sources are shown in black, with associated error bars. In order of increasing wavelength, the squares are from the 1.1–1.9 μm *HST*/NICMOS analysis of Pont et al. (2009) plotted at 1.5 μm; the ground-based *H*-band data of Alonso et al. (2008) plotted at 1.6 μm; the ground-based K_s band data of Cáceres et al. (2009) plotted at 2.1 μm, as discussed by Knutson et al. (2011); and the *Spitzer*/IRAC analysis of Knutson et al. (2011) plotted at 3.6, 4.5, and 8 μm. The diamonds are from the *Spitzer* analysis of Beaulieu et al. (2011) at 3.6, 4.5, and 8 μm. The triangles are the *Spitzer* transits at 3.6 and 4.5 μm that Knutson et al. (2011) suggest are influenced by the occultation of star spots or other regions of non-uniform brightness on the star. The black dotted curves at the bottom show the response functions for the filters and/or detector channels used in the observations. The colored circles represent the corresponding model transit depths averaged over the appropriate filters/channels.

(A color version of this figure is available in the online journal.)

The higher the atmospheric metallicity, the higher the mean molecular weight, and the smaller the atmospheric scale height for any given temperature and gravity profile. High-metallicity atmospheres will then have flatter transmission spectra (e.g., Miller-Ricci et al. 2009; Fortney et al. 2013). Examples of transmission spectra from some of our GJ 436b models are shown in Figure 17, in comparison with observations. The relatively flat spectrum observed in *HST*/NICMOS data (Pont et al. 2009; Gibson et al. 2011) seems more consistent with the

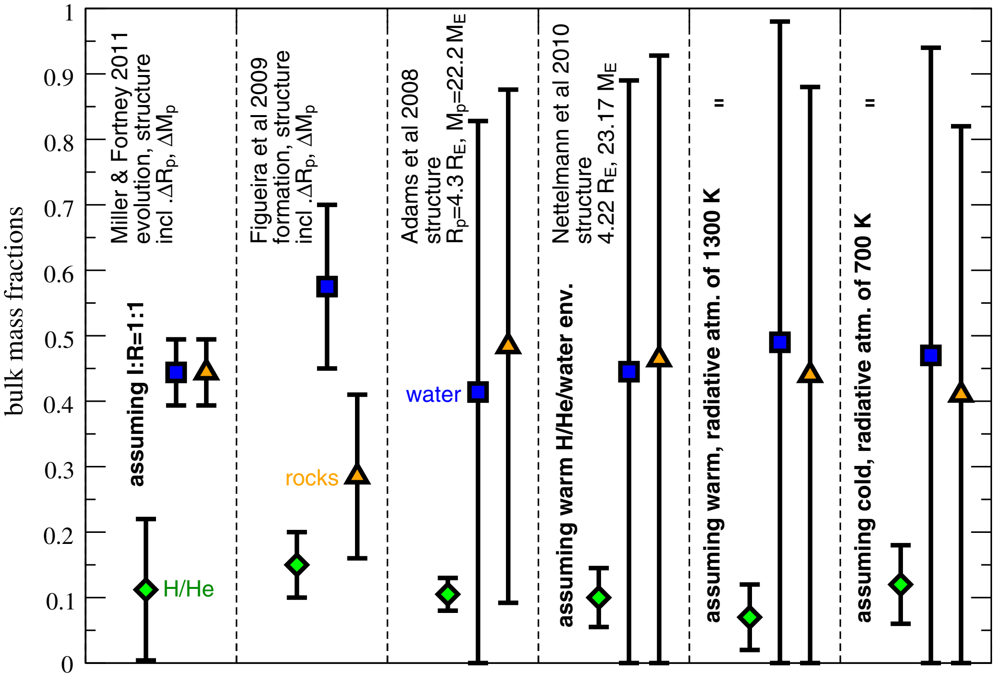

Figure 18. Constraints on the bulk composition of GJ 436b as determined from models of its structure, evolution, and formation. Possible compositions are shown for six different model assumptions and/or imposed constraints. For each, the sum over the displayed mass fractions of H/He (green diamonds), water (blue squares), and "rock" (includes silicates plus iron; orange triangles) equals 1. All calculations take into account the planet's mass M_p and radius R_p as one set of constraints; the two leftmost models consider uncertainties in M_p and R_p, which expands the possible H/He mass fraction by a factor of ~2, while the four on the right adopt specific M_p and R_p values from Torres et al. (2008). From left to right, the derived constraints are based on (1) the thermal and structural evolution models of Miller & Fortney (2011) that assume an ice:rock ratio of 1:1 and that impose constraints based on the age of the GJ 436 system; (2) the formation, disk–planet evolution (including migration), and structural models of Figueira et al. (2009) that compute various formation paths consistent with M_p and R_p; (3) the structure models of Adams et al. (2008) that consider precise values for M_p, R_p, and atmospheric temperatures and thus derive a smaller range of acceptable H/He values; (4) the structural models of Nettelmann et al. (2010) that assume that water is mixed into the outermost H/He envelope; (5) structural models based on Nettelmann et al. (2010) that assume that a pure H/He layer resides above a water layer with a warm (1300 K) deep isothermal radiative region; (6) a model similar to the one on the immediate left, except the isothermal radiative region is cool (700 K) and the planet is old (>10 Gyr). Note from comparing the latter two models that atmospheric temperatures affect the derived H/He mass fraction.

(A color version of this figure is available in the online journal.)

high-metallicity models (see also H. A. Knutson et al. 2013, in preparation, for comparisons with recent *HST*/WFC3 data, which are also quite flat in the 1.1–1.6 μm region), and such models also seem to compare well to the results from the Knutson et al. (2011) *Spitzer* transit analysis (see the open squares at 3.6, 4.5, and 8 μm in Figure 17). However, the high-metallicity models do not compare well with the Beaulieu et al. (2011) *Spitzer* transit analysis (see the open diamonds in Figure 17) or the K_s-band transit data of Cáceres et al. (2009), and in fact none of the models provides a reasonable fit to all the available transit data for GJ 436b. Given the observed variability in the apparent transit depths with time from different observations (e.g., Knutson et al. 2011) and the lack of agreement between transit results analyzed with different procedures (e.g., Pont et al. 2009; Gibson et al. 2011; Knutson et al. 2011; Beaulieu et al. 2011), the poor fits of these models to the transit data are not particularly surprising. Obtaining simultaneous spectral observations at multiple wavelengths should help resolve some of these issues and help distinguish between competing models (see also Benneke & Seager 2013).

Note that we have not adjusted for potential differences in temperatures or chemical abundances between the terminator and dayside atmospheres when performing these calculations. The dayside atmosphere observed at secondary eclipse is likely hotter than the limb atmosphere at the terminators probed in the planetary transit (see Lewis et al. 2010). The non-negligible eccentricity of GJ 436b will also lead to variations in temperature over the orbit, which is captured in the GCMs of Lewis et al. (2010). It is likely that horizontal quenching will help homogenize the atmospheric abundances with respect to longitude due to strong zonal winds or rapid thermal changes over the orbit (Cooper & Showman 2006; Iro & Deming 2010; Visscher 2012; Agúndez et al. 2012), but without more detailed multi-dimensional and temporal modeling, it is difficult to predict the exact terminator composition. Regardless of the exact molecular composition, however, the high-metallicity models will have a higher atmospheric mean molecular mass, and a flatter overall transit spectrum.

4. GJ 436b COMPOSITIONAL CONSTRAINTS FROM STRUCTURE AND EVOLUTION MODELS

As mentioned earlier, a relatively high metallicity for GJ 436b is also indicated by the planet's observed radius in relation to its mass. Figure 18 shows some of the compositional constraints imposed by models of the planet's interior structure, formation, and evolution (e.g., Adams et al. 2008; Baraffe et al. 2008; Figueira et al. 2009; Rogers & Seager 2010a; Nettelmann et al. 2010; Miller & Fortney 2011). The amount of H/He required to explain the mass and radius of GJ 436b depends on several other assumptions in the models, such as the relative abundance of ices (i.e., volatile heavy elements) versus rocks (i.e., refractory heavy elements), the age and evolutionary history of the planet, the presence/absence of a central core, the degree of mixing of elements within the planet, and the thermal structure within the planet. The different interior models typically consider a different variety of assumptions, as explained in the caption to Figure 18. Not much H/He is needed to explain the observed radius if the planet is very hot (i.e., young, high intrinsic interior $T_{\rm int}$ or tidal heating, early onset of convective interior, high-temperature isothermal radiative region), if the heavy elements in the planet have low atomic weight (i.e., ices, not rocks), and/or if the heavy elements are confined to deep levels and are not mixed throughout the atmospheric envelope. Conversely, more H/He is needed to explain the radius if the planet is old and cool, contains more rocky than icy elements, and has heavy elements mixed throughout the atmospheric envelope. Parameters such as the ice-to-rock ratio of GJ 436b are not well constrained from structure and evolution models alone, and uncertainties associated with the planet's age, mass, radius, evolutionary history, and atmospheric and interior thermal structure all contribute to uncertainties in the derived H/He mass fraction on GJ 436b.

Accounting for the various uncertainties and adopting reasonable assumptions about the atmosphere and interior, most of these models predict H/He mass fractions of ∼3%–22% for GJ 436b, corresponding to metallicities of ∼230–2000 times solar. Nettelmann et al. (2010) demonstrate that even lower H/He mass fractions (higher metallicities) are possible (see Figure 18) if the planet contains few rocky elements (only ices), if the ices are confined to the core, and if the pure H/He outer envelope is hot as a result of a thin radiative region. A hot isothermal radiative region is possible for GJ 436b (see Spiegel et al. 2010 and our Figure 1 above); however, the other assumptions in the very-low H/He mass-fraction models are less secure, and given that the secondary-eclipse data show evidence for molecular absorbers rather than a blackbody atmosphere, it seems likely that at least some heavy "icy" elements are mixed into the outer atmospheric envelope. Therefore, the ∼230–2000 times solar models seem most probable for GJ 436b, and our high-metallicity disequilibrium models discussed in Section 3.3 appear reasonable in terms of the interior and evolution models for GJ 436b.

5. POTENTIAL CLOUD FORMATION ON GJ 436b

Clouds have been neglected in our GJ 436b retrievals and forward spectral models, and cloud-microphysical processes such as gravitational settling have been neglected in our chemical models. This neglect is simply a matter of convenience and is not meant to be an indictment of the importance of clouds and their related influence on atmospheric properties. Condensates are expected to form in the atmospheres of GJ 436b and other hot Neptunes, and although we leave detailed cloud models to future investigations, we briefly comment here on the major cloud components that could potentially affect photospheric properties on GJ 436b.

The equilibrium cloud condensation sequence in hydrogen-dominated extrasolar giant planet atmospheres has been well studied (e.g., Morley et al. 2012, 2013 and references therein). Our chemical-equilibrium model reproduces these standard clouds and predicts that the most refractory clouds, such as Ca-, Al-, and Ti-oxides and -silicates, Fe-metal, Mg-silicates, Cr-metal, and MnS condense well below the photosphere for all GJ 436b models considered, regardless of the assumed atmospheric metallicity. Less refractory species such as sodium sulfide (Na_2S) and KCl are potentially important condensates within the photosphere. Because the elements Na and S are more abundant than K and Cl, the Na_2S cloud is expected to be roughly an order of magnitude more important in terms of total available cloud mass than the KCl cloud. Another potential photospheric cloud on hot Neptunes is ZnS (e.g., Visscher et al. 2006; Morley et al. 2013), although we have not included Zn in our equilibrium calculations because it is a less-abundant element.

For the 1 times solar model (thermal structure shown in Figure 1), Na_2S first condenses at the 633 mbar, 966 K level in our relatively broad model grid, and KCl first condenses at the 194 mbar, 750 K grid point. The sodium vapor pressure over solid Na_2S is large enough within the few-hundred millibar region that some sodium remains available for NaCl condensation at 194 mbar, 750 K in these models. Judging from the Morley et al. (2013) calculations, these equilibrium condensation clouds will not have a sufficiently large slant optical depth at sufficiently high altitudes at the terminators to obscure gas-phase molecular features in the transmission spectra. Given that the slant optical depth is a factor of ∼20 larger than the vertical optical depth (Fortney 2005), it is also unlikely that these clouds would affect the emission spectra for the 1 times solar models, despite their potential presence in the photosphere. Higher metallicities can change this picture, however (e.g., Morley et al. 2013). Convenient expressions that predict the condensation location as a function of pressure, temperature, and atmospheric metallicity are found in Morley et al. (2012) for KCl clouds and in Visscher et al. (2006) for Na_2S (and ZnS) clouds, although caution should be used in extrapolating these expressions outside the intended metallicity range of $10^{-0.5}$–$10^{0.5}$ times solar.

For our 50 times solar GJ 436b model (see Figure 1), Na_2S first condenses even deeper (at the 42.5 bar, 1382 K grid point), and the Na_2S cloud would be too deep affect spectra. The KCl condensation curve, on the other hand, nicely tracks the photosphere as the metallicity changes, and KCl first condenses at 27 mbar, 793 K in our 50 times solar model. Judging from the information in Morley et al. (2013), the enhanced elemental abundances in this model could lead to optical depths for the KCl (and ZnS) clouds that could potentially affect transit spectra. This 50 times solar model, however, is unlikely to be relevant to the actual GJ 436b due to the high predicted CH_4 abundance, among other issues (see Section 3.3). For our 1000× solar GJ 436b model (see Figure 1), Na_2S again condenses deep enough to be irrelevant to the transit and eclipse spectra, but KCl condenses at 8.8 mbar, 839 K, and KCl clouds would again need to be considered if this model were relevant. Judging from Visscher et al. (2006) and Morley et al. (2013), ZnS clouds could also be important in the 1000 times solar-metallicity model. Our favored model presented in Figures 15 and 16 has a metallicity of 300 times solar and a C/O ratio of 0.6. The altered C/O ratio can have some effect on the predicted condensation levels in these models, but Na_2S condenses too deep to affect spectra, while KCl condenses at 5.5 mbar, 781 K and could conceivably affect the predicted transit and eclipse spectra; further cloud-opacity calculations are therefore warranted for this case but are left to future investigations. Note that KCl is the dominant potassium-bearing gas at these pressure levels, so there should be no gas-phase kinetic barriers to KCl condensation. The same cannot be said for the potential ZnS cloud, which would form via the net equilibrium reaction $H_2S + Zn \leftrightarrow ZnS(solid) + H_2$ (Visscher et al. 2006). Because sulfur might be liberated relatively easily from H_2S by photolysis at these pressure levels, ZnS formation should not be too problematic.

Graphite condensation is more of a wild card in the cloud condensation sequence, as its stability is more sensitive to conditions such as the C/O ratio and metallicity, and the chemical kinetics involved with its formation could be complex enough that graphite condensation is not a foregone conclusion, even within atmospheric regions where it would be thermochemically stable. Not only must the gas density be high enough that grains form on a time scale shorter than the transport of the gas away from the graphite-stability regions (see, e.g., Sharp & Wasserburg 1995), but the carbon must be relinquished from its gas-phase confines within a similar reasonable time frame. For our 1 times and 50 times solar GJ 436b models, graphite never becomes stable. For our 1000 times solar model, graphite is theoretically stable at very high altitudes (7 μbar, 560 K), but any grains that form there would rapidly settle out gravitationally to lower-altitude regions where graphite is not stable. It is therefore very unlikely that a sufficiently optically thick column of graphite grains would build up to affect spectra. For any fixed bulk C/O ratio, a higher atmospheric metallicity allows the graphite stability field to generally expand to higher temperature and pressure regions along the atmospheric profile, making graphite clouds more likely at higher metallicities, but to maintain graphite grains in the planet's photosphere, super-solar C/O ratios are likely needed.

In our favored GJ 436b model with a 300 times solar-metallicity and super-solar C/O ratio of 0.6, graphite is thermochemically stable within the photosphere (i.e, with a potential cloud base at ∼4 mbar, 729 K). Tiny graphite grains would survive longer at these pressures and could conceivably affect spectra. However, thermodynamic stability and long gravitational settling times are not sufficient enough conditions for grain formation to occur. At the relevant altitude levels, carbon is predominantly tied up in relatively oxidized species like gaseous CO and CO_2. Kinetic conversion between oxidized and reduced forms of carbon has long shut down as a result of transport-induced quenching (see Section 2.1 or Moses 2013), and it seems unlikely that the carbon in CO and CO_2 could be kinetically converted to condensed graphite on time scales shorter than the vertical (or horizontal) transport time scales. However, due to the potential spectral importance of graphite clouds in hot-Neptune atmospheres, the topic of the kinetics, nucleation, and condensation of graphite grains deserves further study. If graphite condensation does not occur, the contours in Figures 5, 6, and 11 will be affected, and the photospheric gas-phase C/O ratio could conceivably exceed 1. We leave such studies to future investigations.

6. CONCLUSIONS

Moderate-to-high metallicity models (∼230–2000 times solar) for GJ 436b are appealing in that they provide a natural explanation for the apparent CO-rich, CH_4-poor nature of GJ 436b's atmosphere (see Stevenson et al. 2010; Madhusudhan & Seager 2011) and are consistent with the heavy-element enrichment as inferred from the planet's mass and radius from interior modeling (Adams et al. 2008; Baraffe et al. 2008; Figueira et al. 2009; Rogers & Seager 2010a; Nettelmann et al. 2010). Although such high-metallicity models are not without problems in terms of explaining all the transit and secondary-eclipse data (see Section 3.3), they do have one significant advantage over the best-fit solutions obtained to date from retrieval methods (e.g., Madhusudhan & Seager 2011 and Section 3.2 above)—the advantage of physical and chemical plausibility. The best-fit solutions from the retrievals imply an atmosphere dominated by H_2 and CO, with a low water abundance and a very low methane abundance. Carbon monoxide in an H_2-rich atmosphere without the presence of either water or methane is problematic from a theoretical standpoint, and the relative abundances of CO, H_2O, CH_4, and CO_2 derived for GJ 436b from the solutions favored by the retrievals do not appear to be achievable from either equilibrium or disequilibrium chemistry in a GJ 436b atmosphere with any plausible imagined bulk properties (i.e., metallicity, C/O ratio, temperature). Either our theoretical understanding is incomplete, and we are missing some key disequilibrium mechanisms that convert CH_4 and H_2O permanently to CO in GJ 436b's dayside atmosphere, or the retrieved solutions simply reflect some of the pitfalls that arise when applying retrieval methods (and their built-in assumptions) to sparse data sets with large systematic uncertainties (e.g., Line et al. 2013).

Retrievals are powerful, but problems can arise if data uncertainties have been underestimated or if the built-in assumptions (e.g., the parameterizations controlling the shape of the temperature profile or the list of potential opacity sources, including clouds) are incorrect or incomplete. From that standpoint, it would be useful if the error bars provided for transit and eclipse observations accurately reflected systematic uncertainties inherent with the instruments, along with the more commonly reported statistical uncertainties. Failing that, instrument systematics could be considered when performing the retrievals, and/or the list of opacity sources considered in the retrievals could be expanded. Forward models are also not without potential sources of error, so it is possible that some as-yet-undiscovered chemical mechanism could provide an explanation for the apparent CO-rich, water- and methane-poor composition of GJ 436b.

To make further progress on characterizing the atmosphere of GJ 436b (and other hot Neptunes), we would need additional transit and eclipse data, preferably from a space-based instrument that can deliver spectra at multiple wavelengths simultaneously. Given the observed variability in the GJ 436b transit depths from one transit to the next (Knutson et al. 2011), which might be related to the occultation of star spots, obtaining simultaneous wavelength information is desirable for transit observations. If hot-Netpune exoplanets do indeed have higher metallicities than is typical for hot Jupiters, as we suggest, then the transmission spectra from hot Neptunes would be flatter and more featureless in general, even in the absence of photospheric clouds. Figure 17 shows that transit observations with moderate spectral resolution in the 1–5 μm region should help distinguish between the low- or high-metallicity scenarios, with the relative transit depth at ∼3.5 μm versus 4.5 μm being particularly diagnostic. Emission spectra from secondary-eclipse observations have some advantages over transit observations in terms of characterizing atmospheres, despite the well-known problems with degeneracies between temperatures and abundances (e.g., Burrows & Orton 2010), because more information can be derived with respect to atmospheric temperatures, the emission measurements tend to be less sensitive to vertically-thin scattering clouds and hazes, and the planetary flux can compete with the stellar flux at mid-IR wavelengths where many molecules have diagnostic features. In that regard, having a space-based infrared telescope that extends to ∼16 μm, like EChO (Tinetti et al. 2012), could be critical for correctly diagnosing atmospheric properties (e.g., Tinetti et al. 2012; Barstow et al. 2013).

Regardless of whether GJ 436b itself has a high-metallicity atmosphere, radial-velocity and transit surveys show that Neptune-class exoplanets are exceedingly common in the galaxy

(Howard et al. 2010, 2012; Mayor et al. 2011; Borucki et al. 2011; Batalha et al. 2013), and based on our current views of exoplanet formation (see Section 3.1), we would expect many of these planets to have atmospheric metallicities that are orders of magnitude in excess of solar. There is some evidence for that trend in the existing population of exoplanets for which we have derivations of both mass and radius (e.g., Miller & Fortney 2011; Weiss et al. 2013; Wu et al. 2013). As is shown in Figures 4, 5, and 6, hot Neptunes could have very diverse atmospheric compositions depending on atmospheric temperatures and bulk atmospheric properties such as metallicity and C/O ratio. The higher-metallicity atmospheres described in this paper have no analogs from within our own solar system, but one can imagine a continuum of hot Neptunes that should exist in the exoplanet population, with atmospheres ranging from moderate-to-low metallicity, hydrogen-rich, Neptune-like compositions to high-metallicity, hydrogen-poor, super-Venus-like compositions, along with more exotic CO-dominated planets and H_2O-dominated "water worlds." As the statistics regarding exoplanet properties continues to grow, so does our amazement at the diversity of these worlds beyond the narrow confines of our solar system.

We thank Nikole Lewis for providing her dayside-average GCM thermal profiles for GJ 436b and for motivating the cloud discussion, Heather Knutson for several illuminating conversations in relation to the paper and her latest GJ 436b transit data, and the anonymous reviewer for a thorough manuscript review and useful suggestions (and additional motivation for the cloud discussion). This work was supported by the NASA Planetary Atmospheres Program grant number NNX11AD64G.

REFERENCES

Adams, E. R., Seager, S., & Elkins-Tanton, L. 2008, ApJ, 673, 1160
Agúndez, M., Venot, O., Iro, N., et al. 2012, A&A, 548, A73
Alibert, Y., Baraffe, I., Benz, W., et al. 2006, A&A, 455, L25
Alibert, Y., Mordasini, C., Benz, W., & Winisdoerffer, C. 2005, A&A, 434, 343
Allard, F., Hauschildt, P. H., Alexander, D. R., Tamanai, A., & Schweitzer, A. 2001, ApJ, 556, 357
Allen, M., Yung, Y. L., & Waters, J. W. 1981, JGR, 86, 3617
Alonso, R., Barbieri, M., Rabus, M., et al. 2008, A&A, 487, L5
Atkinson, R., Baulch, D. L., Cox, R. A., et al. 2004, ACP, 4, 1461
Atkinson, R., Baulch, D. L., Cox, R. A., et al. 2006, ACP, 6, 3625
Baines, K. H., Mickelson, M. E., Larson, L. E., & Ferguson, D. W. 1995, Icar, 114, 328
Ballard, S., Christiansen, J. L., Charbonneau, D., et al. 2010, ApJ, 716, 1047
Baraffe, I., Chabrier, G., & Barman, T. 2008, A&A, 482, 315
Barman, T. S., Hauschildt, P. H., & Allard, F. 2001, ApJ, 556, 885
Barman, T. S., Hauschildt, P. H., & Allard, F. 2005, ApJ, 632, 1132
Barstow, J. K., Aigrain, S., Irwin, P. G. J., et al. 2013, MNRAS, 430, 1188
Batalha, N. M., Rowe, J. F., Bryson, S. T., et al. 2013, ApJS, 204, 24
Bean, J. L., Benedict, G. F., Charbonneau, D., et al. 2008, A&A, 486, 1039
Bean, J. L., Benedict, G. F., & Endl, M. 2006, ApJL, 653, L65
Beaulieu, J.-P., Tinetti, G., Kipping, D. M., et al. 2011, ApJ, 731, 16
Benneke, B., & Seager, S. 2012, ApJ, 753, 100
Benneke, B., & Seager, S. 2013, arXiv:1306.6325
Bézard, B., Lellouch, E., Strobel, D., Maillard, J.-P., & Drossart, P. 2002, Icar, 159, 95
Bodenheimer, P. H., & Pollack, J. B. 1986, Icar, 67, 391
Borucki, W. J., Koch, D. G., Basri, G., et al. 2011, ApJ, 736, 19
Burrows, A., & Orton, G. 2010, in Exoplanets, ed. S. Seager (Tucson, AZ: Univ. Arizona Press), 419
Butler, R. P., Vogt, S. S., Marcy, G. W., et al. 2004, ApJ, 617, 580
Cáceres, C., Ivanov, V. D., Minniti, D., et al. 2009, A&A, 507, 481
Cooper, C. S., & Showman, A. P. 2006, ApJ, 649, 1048
Coughlin, J. L., Stringfellow, G. S., Becker, A. C., et al. 2008, ApJL, 689, L149
Deming, D., Harrington, J., Laughlin, G., et al. 2007, ApJL, 667, L199
Demory, B.-O., Gillon, M., Barman, T., et al. 2007, A&A, 475, 1125
Ehrenreich, D., Lecavelier des Etangs, A., & Delfosse, X. 2011, A&A, 529, A80
Elkins-Tanton, L. T., & Seager, S. 2008, ApJ, 685, 1237
Fegley, B., Jr., Gautier, D., Owen, T., & Prinn, R. G. 1991, in Uranus, ed. J. T. Bergstrahl, E. D. Miner, & M. Shapley Matthews (Tucson, AZ: Univ. Arizona Press), 147
Fegley, B., Jr., & Lodders, K. 1994, Icar, 110, 117
Figueira, P., Pont, F., Mordasini, C., et al. 2009, A&A, 493, 671
Fortney, J. J. 2005, MNRAS, 364, 649
Fortney, J. J., Marley, M. S., & Barnes, J. W. 2007, ApJ, 659, 1661
Fortney, J. J., Mordasini, C., Nettelmann, N., Kempton, E., & Zahnle, K. 2013, ApJ, 775, 80
Fortney, J. J., & Nettelmann, N. 2010, SSRv, 152, 423
Fortney, J. J., Saumon, D., Marley, M. S., Lodders, K., & Freedman, R. S. 2006, ApJ, 642, 495
Fouchet, T., Moses, J. I., & Conrath, B. J. 2009, in Saturn from Cassini-Huygens, ed. M. K. Dougherty, L. W. Esposito, & S. M. Krimigis (Dordrecht: Springer), 83
France, K., Froning, C. S., Linsky, J. L., et al. 2013, ApJ, 763, 149
Fressin, F., Torres, G., Charbonneau, D., et al. 2013, ApJ, 766, 81
Gaidos, E. 2012, Abstract Presented at Comparative Climatology of Terrestrial Planets (Houston, TX: LPI)
García Muñoz, A. 2007, P&SS, 55, 1426
Gautier, D., Conrath, B. J., Owen, T., de Pater, I., & Atreya, S. K. 1995, in Neptune and Triton, ed. D. P. Cruikshank (Tucson, AZ: Univ. Arizona Press), 547
Gibson, N. P., Pont, F., & Aigrain, S. 2011, MNRAS, 411, 2199
Gillon, M., Demory, B.-O., Barman, T., et al. 2007a, A&A, 471, L51
Gillon, M., Pont, F., Demory, B.-O., et al. 2007b, A&A, 472, L13
Gordon, S., & McBride, B. J. 1994, NASA Reference Publication, 131
Guillot, T. 2010, A&A, 527, A27
Hansen, B., & Murray, N. 2012, ApJ, 751, 158
Hauschildt, P. H., & Baron, E. 1999, JCoAM, 109, 41
Hawley, S. L., Gizis, J. E., & Reid, I. N. 1996, AJ, 112, 2799
Heap, S., & Lindler, D. 2010, http://archive.stsci.edu/pub/hlsp/stisngsl/
Howard, A. W., Marcy, G. W., Bryson, S. T., et al. 2012, ApJS, 201, 15
Howard, A. W., Marcy, G. W., Johnson, J. A., et al. 2010, Sci, 330, 653
Hu, R., Seager, S., & Bains, W. 2012, ApJ, 761, 166
Hubbard, W. B., Podolak, M., & Stevenson, D. J. 1995, in Neptune and Triton, ed. D. P. Cruikshank (Tucson, AZ: Univ. Arizona Press), 109
Iro, N., & Deming, L. D. 2010, ApJ, 712, 218
Jenkins, J. S., Ramsey, L. W., Jones, H. R. A., et al. 2009, ApJ, 704, 975
Karkoschka, E., & Tomasko, M. 2009, Icar, 202, 287
Karkoschka, E., & Tomasko, M. 2011, Icar, 211, 780
Kirkpatrick, J. D., Henry, T. J., & McCarthy, D. W., Jr. 1991, ApJS, 77, 417
Kite, E. S., Manga, M., & Gaidos, E. 2009, ApJ, 700, 1732
Knutson, H. A., Howard, A. W., & Isaacson, H. 2010, ApJ, 720, 1569
Knutson, H. A., Madhusudhan, N., Cowan, N. B., et al. 2011, ApJ, 735, 27
Kopparapu, R. K., Kasting, J. F., & Zahnle, K. J. 2012, ApJ, 745, 77
Kuchner, M. J., & Seager, S. 2005, arXiv:astro-ph/0504214
Lee, J.-M., Fletcher, L. N., & Irwin., P. G. J. 2012, MNRAS, 420, 170
Lewis, J. S., & Fegley, B., Jr. 1984, SSRv, 39, 163
Lewis, N. K., Showman, A. P., Fortney, J. J., et al. 2010, ApJ, 720, 344
Liang, M.-C., Parkinson, C. D., Lee, A. Y. T., Yung, Y. L., & Seager, S. 2003, ApJL, 596, L247
Liang, M.-C., Seager, S., Parkinson, C. D., Lee, A. Y. T., & Yung, Y. L. 2004, ApJL, 605, L61
Lindzen, R. S. 1981, JGR, 86, 9707
Line, M. R., Liang, M. C., & Yung, Y. L. 2010, ApJ, 717, 496
Line, M. R., Vasisht, G., Chen, P., Angerhausen, D., & Yung, Y. L. 2011, ApJ, 738, 32
Line, M. R., Wolf, A. S., Zhang, X., et al. 2013, arXiv:1304.5561
Line, M. R., Zhang, X., Vasisht, G., et al. 2012, ApJ, 749, 93
Lissauer, J. J., & Stevenson, D. J. 2007, in Protostars and Planets V, ed. B. Reipurth, D. Jewitt, & K. Keil (Tucson, AZ: Univ. Arizona Press), 591
Lodders, K. 2004, ApJ, 611, 587
Lodders, K. 2010, in Formation and Evolution of Exoplanets, ed. R. Barnes (Berlin: Wiley), 157
Lodders, K., & Fegley, B., Jr. 1994, Icar, 112, 368
Lodders, K., & Fegley, B., Jr. 1997, in AIP Conf. Proc. 402, Astrophysical Implications of the Laboratory Study of Presolar Materials, ed. T. J. Bernatowicz & E. Zinner (Melville, NY: AIP), 391
Lodders, K., & Fegley, B., Jr. 2002, Icar, 155, 393
Lodders, K., Palme, H., & Gail, H.-P. 2009, in The Solar System, Landolt-Börnstein, New Series, Vol. VI/4B, ed. J. E. Trümper (Berlin: Springer), 560
Luszcz-Cook, S. H., & de Pater, I. 2013, Icar, 222, 379
Madhusudhan, N. 2012, ApJ, 758, 36
Madhusudhan, N., Harrington, J., Stevenson, K. B., et al. 2011a, Natur, 469, 64

Madhusudhan, N., Mousis, O., Johnson, T. V., & Lunine, J. I. 2011b, ApJ, 743, 191

Madhusudhan, N., & Seager, S. 2009, ApJ, 707, 24

Madhusudhan, N., & Seager, S. 2011, ApJ, 729, 41

Maness, H. L., Marcy, G. W., Ford, E. B., et al. 2007, PASP, 119, 90

Marley, M. S., Fortney, J. J., Hubickyj, O., Bodenheimer, P., & Lissauer, J. J. 2007, ApJ, 655, 541

Mayor, M., Marmier, M., Lovis, C., et al. 2011, arXiv:1109.2497

Miguel, Y., Kaltenegger, L., Fegley, B., Jr., & Schaefer, L. 2011, ApJL, 742, L19

Miller, J. A., Klippenstein, S. J., Robertson, S. H., Pilling, M. J., & Green, N. J. B. 2009, Phys. Chem. Chem. Phys., 11, 1128

Miller, N., & Fortney, J. J. 2011, ApJL, 736, L29

Miller-Ricci, E., & Fortney, J. J. 2010, ApJL, 716, L74

Miller-Ricci, E., Seager, S., & Sasselov, D. 2009, ApJ, 690, 1056

Miller-Ricci Kempton, E., Zahnle, K., & Fortney, J. 2012, ApJ, 745, 3

Mills, F. P. 1998, PhD thesis, Caltech

Mizuno, H., Nakazawa, K., & Hayashi, C. 1978, PThPh, 60, 699

Mordasini, C., Alibert, Y., Georgy, C., et al. 2012a, A&A, 547, A112

Mordasini, C., Alibert, Y., Klahr, H., & Henning, T. 2012b, A&A, 547, A111

Morley, C. V., Fortney, J. J., Kempton, E. M.-R., et al. 2013, ApJ, 775, 33

Morley, C. V., Fortney, J. J., Marley, M. S., et al. 2012, ApJ, 756, 172

Moses, J. I. 2013, RSPTA, in press (arXiv:1307.5450)

Moses, J. I., Fouchet, T., Yelle, R. V., et al. 2004, in Jupiter: The Planet, Satellites & Magnetosphere, ed. F. Bagenal, T. E. Dowling, & W. B. McKinnon (Cambridge: Cambridge Univ. Press), 129

Moses, J. I., Madhusudhan, N., Visscher, C., & Freedman, R. S. 2013, ApJ, 763, 25

Moses, J. I., Visscher, C., Fortney, J. J., et al. 2011, ApJ, 737, 15

Moses, J. I., Visscher, C., Keane, T. C., & Sperier, A. 2010, FaDi, 147, 103

Mousis, O., Lunine, J. I., Madhusudhan, N., & Johnson, T. V. 2012, ApJL, 751, L7

Mousis, O., Lunine, J. I., Petit, J.-M., et al. 2011, ApJ, 727, 77

Nettelmann, N., Fortney, J. J., Kramm, U., & Redmer, R. 2011, ApJ, 733, 2

Nettelmann, N., Helled, R., Fortney, J. J., & Redmer, R. 2013, P&SS, 77, 143

Nettelmann, N., Kramm, U., Redmer, R., & Neuhäuser, R. 2010, A&A, 523, A26

Öberg, K. I., Murray-Clay, R., & Bergin, E. A. 2011, ApJL, 743, L16

Parmentier, V., Showman, A. P., & Lian, Y. 2013, arXiv:1301.4522

Podolak, M., Weizman, A., & Marley, M. 1995, P&SS, 43, 1517

Pollack, J. B., Hubickyj, O., Bodenheimer, P., et al. 1996, Icar, 124, 62

Pont, F., Gilliland, R. L., Knutson, H., Holman, M., & Charbonneau, D. 2009, MNRAS, 393, L6

Prinn, R. G., & Barshay, S. S. 1977, Sci, 198, 1031

Richardson, M. R., Moses, J. I., Line, M. R., et al. 2013, 44th Lunar and Planetary Science Conference (Houston, TX: LPI), 2678

Rogers, L. A., Bodenheimer, P., Lissauer, J. J., & Seager, S. 2011, ApJ, 738, 59

Rogers, L. A., & Seager, S. 2010a, ApJ, 712, 974

Rogers, L. A., & Seager, S. 2010b, ApJ, 716, 1208

Saffe, C., Gómez, M., & Chavero, C. 2005, A&A, 443, 609

Sander, S. P., Abbatt, J. P. D., Barker, J. R., et al. 2011, Chemical Kinetics and Photochemical Data for Use in Atmospheric Studies. Evaluation Number 17, JPL Publication 10-6 (Pasadena, CA: NASA)

Sanz-Forcada, J., Micela, G., Ribas, I., et al. 2011, A&A, 532, A6

Sanz-Forcada, J., Ribas, I., Micela, G., et al. 2010, A&A, 511, L8

Schaefer, L., & Fegley, B., Jr. 2009, ApJL, 703, L113

Schaefer, L., Lodders, K., & Fegley, B., Jr. 2012, ApJ, 755, 41

Seager, S., Richardson, L. J., Hansen, B. M. S., et al. 2005, ApJ, 632, 1122

Segura, A., Meadows, V. S., Kasting, J. F., Crisp, D., & Cohen, M. 2007, A&A, 472, 665

Selsis, F., Despois, D., & Parisot, J.-P. 2002, A&A, 388, 985

Shabram, M., Fortney, J. J., Greene, T. P., & Freedman, R. S. 2011, ApJ, 727, 65

Sharp, C. M., & Burrows, A. 2007, ApJS, 168, 140

Sharp, C. M., & Wasserburg, G. J. 1995, GeCoA, 59, 1633

Showman, A. P., Fortney, J. J., Lian, Y., et al. 2009, ApJ, 699, 564

Shporer, A., Mazeh, T., Pont, F., et al. 2009, ApJ, 694, 1559

Southworth, J. 2010, MNRAS, 408, 1689

Spiegel, D. S., Burrows, A., Ibgui, L., Hubeny, I., & Milsom, J. A. 2010, ApJ, 709, 149

Stevenson, K. B., Harrington, J., Lust, N. B., et al. 2012, ApJ, 755, 9

Stevenson, K. B., Harrington, J., Nymeyer, S., et al. 2010, Natur, 464, 1161

Stone, P. H. 1976, in Jupiter, ed. T. Gehrels (Tucson, AZ: Univ. Arizona Press), 586

Tinetti, G., Beaulieu, J. P., Henning, T., et al. 2012, ExA, 34, 311

Torres, G., Winn, J. N., & Holman, M. J. 2008, ApJ, 677, 1324

Venot, O., Fray, N., Bénilan, Y., et al. 2013, A&A, 551, A131

Venot, O., Hébrard, G., Agúndez, M., et al. 2012, A&A, 546, A43

Visscher, C. 2012, ApJ, 757, 5

Visscher, C., Lodders, K., & Fegley, B., Jr. 2006, ApJ, 648, 1181

Visscher, C., Lodders, K., & Fegley, B., Jr. 2010a, ApJ, 716, 1060

Visscher, C., & Moses, J. I. 2011, ApJ, 738, 72

Visscher, C., Moses, J. I., & Saslow, S. A. 2010b, Icar, 209, 602

von Braun, K., Boyajian, T. S., Kane, S. R., et al. 2012, ApJ, 753, 171

Weiss, L. M., Marcy, G. W., Rowe, J. F., et al. 2013, ApJ, 768, 14

Woods, T. N., & Rottman, G. J. 2002, in Atmospheres in the Solar System: Comparative Aeronomy, ed. M. Mendillo, A. Nagy, & J. H. Waite (Washington, DC: AGU), 221

Wu, Y., & Lithwick, Y. 2013, ApJ, 772, 74

Yung, Y. L., & DeMore, W. B. 1999, Photochemistry of Planetary Atmospheres (Oxford: Oxford Univ. Press)

Zahnle, K., Marley, M. S., Freedman, R. S., Lodders, K., & Fortney, J. J. 2009, ApJL, 701, L20